

Article

Assessing the Activity of Eastern Himalayan Extensional Structures: Evidence from Low-Temperature Thermochronology of Granitic Rocks from Yadong

Tiankun Xu ^{1,2} , Yalin Li ^{1,*} , Finlay M. Stuart ², Zining Ma ¹, Wenjun Bi ³, Yongyong Jia ¹ and Bo Yang ¹

¹ School of Earth Sciences and Resources, China University of Geosciences, Beijing 100083, China; geoxtk@163.com (T.X.); mznucugb@163.com (Z.M.); 2001200145@cugb.edu.cn (Y.J.); baixuejia1007@163.com (B.Y.)

² Scottish Universities Environmental Research Centre (SUERC), Rankine Avenue, East Kilbride G75 0QF, UK; fin.stuart@glasgow.ac.uk

³ Department of Earth Sciences and Engineering, Taiyuan University of Technology, Taiyuan 030024, China; biwenjun@tyut.edu.cn

* Correspondence: liyalin@cugb.edu.cn

Abstract: The east–west-trending South Tibetan Detachment System (STDS) and north–south-trending rifts (NSTRs) are the two main types of extensional structures that have developed within the Tibetan Plateau during continent–continent collision since the early Cenozoic. They have played significant roles in the evolution of the plateau, but it is unclear how they are related genetically. In the Yadong area of the eastern Himalaya, the NSTRs cross-cut the STDS. Apatite and zircon fission track ages of a leucogranite pluton in the footwall of the two extensional faults can be used to reconstruct the cooling and exhumation history and thereby constrain the activity of extensional structures. The new AFT ages range from 10.96 ± 0.70 to 5.68 ± 0.37 Ma, and the ZFT age is 13.57 ± 0.61 Ma. Track length distributions are unimodal, albeit negatively skewed, with standard deviations between 1.4 and 2.1 μm and mean track lengths between 11.6 and 13.4 μm . In conjunction with previously published datasets, the thermal history of the region is best explained by three distinct pulses of exhumation in the last 16 Ma. The first pulse (16–12 Ma) records a brittle slip on the STDS. The two subsequent pulses are attributed to the movement on the Yadong normal fault. The normal fault initiated at ~ 12 Ma and experienced a pulse of accelerated exhumation between 6.2 and 4.7 Ma, probably reflecting the occurrence of two distinct phases of fault activity within the NSTRs, which were primarily instigated by slab tear of the subducting Indian plate.

Keywords: southern Tibet; low-temperature thermochronology; pecube; extensional structure; exhumation; Yadong region



Citation: Xu, T.; Li, Y.; Stuart, F.M.; Ma, Z.; Bi, W.; Jia, Y.; Yang, B. Assessing the Activity of Eastern Himalayan Extensional Structures: Evidence from Low-Temperature Thermochronology of Granitic Rocks from Yadong. *Minerals* **2024**, *14*, 66. <https://doi.org/10.3390/min14010066>

Academic Editors: Aleksei V. Travin, Ruxin Ding, Honghua Lv and Rong Yang

Received: 31 October 2023

Revised: 22 December 2023

Accepted: 31 December 2023

Published: 5 January 2024



Copyright: © 2024 by the authors. Licensee MDPI, Basel, Switzerland. This article is an open access article distributed under the terms and conditions of the Creative Commons Attribution (CC BY) license (<https://creativecommons.org/licenses/by/4.0/>).

1. Introduction

The Himalayan mountain chain is the largest orogenic belt on Earth, formed by the collision of the Indian and Asian plates since the early Cenozoic [1,2]. The Tibetan Plateau exceeds 2.5 million km^2 and is characterized by an average elevation of approximately 5000 m [3]. Two distinct sets of prominent perpendicular extensional structures are present within the Himalaya–Tibetan Plateau system: the east–west oriented South Tibet Detachment System (STDS) and the north–south-trending rifts (NSTRs) (Figure 1) [4–11].

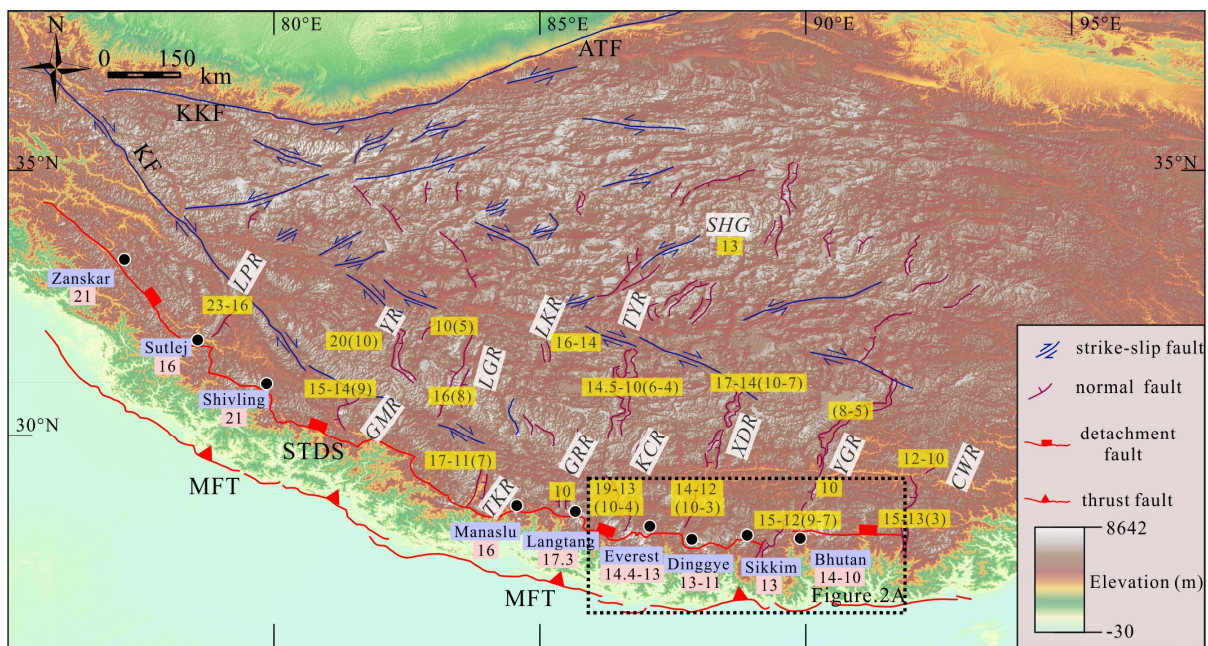


Figure 1. Major fault systems of the Himalayan–Tibetan orogen (modified from Cooper et al. [12]). Digital elevation model generated from the Shuttle Radar Topography Mission 90 m elevation data. The claret line represents north–south-trending normal faults (NSTRs), the violet line represents strike-slip faults, and the red line represents the South Tibetan Detachment System (STDS) and Main Frontal Thrust (MFT). The numbers in the yellow boxes represent estimates for the onset of east–west extension, while the numbers in parentheses indicate the timing of accelerated footwall exhumation. Their units are millions of years (Ma). LPR = Leo Pargil rift [13–15]; GMR = Gurla Mandhata rift [16–18]; YR = Yari rift [19]; LGR = Lunggar rift [20–22]; TKR = Thakkhola rift [23–26]; LKR = Lopukangri Rift [27,28]; GRR = Gyirong rift [29]; KCR = Kung Co rift [1,30,31]; TYR = Tangra Yumco rift [19,32,33]; SHG = Shuanghu graben [34]; XDR = Xainza-Dinggye rift [35–45]; YGR = Yadong–Gulu Rift [12,46–51]; CWR = Cona–Woka Rift [52,53]. The numbers in the light pink boxes represent estimates for the cessation of the STDS locally [40,54–72]. Detailed sample information and references have been listed in Supplementary Table S1. KF = Karakorum fault, ATF = Altyn Tagh fault. The black dashed box represents the area contained in Figure 2A.

The STDS appears as a series of shear zones and normal faults that dip to the north [6,73]. They are present along the entire 2000 km length of the Himalayan topographic crest [74] and appear to separate the Tethyan Himalayan Sequence (THS) to the north from the Greater Himalayan Sequence (GHS) to the south. The exhumation of the GHS is believed to have been closely linked to the movement of the STDS [5,6,75]. Petrochronological analysis of leucogranite bodies located within the shear zone of the STDS reveals that movement occurred predominantly during the Miocene [67,68,76,77]. However, the termination of motion along the detachment system exhibits localized diachroneity [63].

The NSTRs represent the most prominent active tectonic features within the Tibetan Plateau, predominantly manifesting as north–south-trending extensional grabens and sets of high-angle normal faults [78,79]. At least seven main rifts are recognized between 79° E and 92° E. The rifts range from 240 to 500 km in length and are essentially parallel. Their formation and evolution are intimately linked to the uplift of Tibet as well as the adjustment of convergent deformation between the Indian and Eurasian plates [62]. Previous studies have used the time of dyke emplacement or rapid cooling of the footwall to constrain the initiation time of NSTRs, yielding a broad spectrum of temporal estimates as well as the slip rate of faults [13,38,61].

Both sets of structures have played a significant role in accommodating uninterrupted convergence between the Indian and Asian plates, yet it is still unclear how they related mechanically. One view is that the NSTRs were initiated after the cessation of main activity on the STDS. This is based on indications that the NSTRs cross-cut the STDS, as well as geochronological evidence suggesting that the east–west extension occurred after the formation of the STDS in some areas [13,23,36,42,61,80]. However, this view is not supported by age constraints, which imply that the primary period of activity along the STDS was between 25 and 11 Ma [66–68,75,77], while the majority of the activity along the NSTRs occurred between 19 and 3 Ma [30,31,53]. These age constraints suggest that the activity of the two structures occurred simultaneously, at least in some areas. For instance, the STDS and NSTR structures in the Jomolhari region of NW Bhutan had a protracted and overlapping deformation history around 14 Ma [12,65]. Geochronological data from the Ama Drime Massif (ADM) indicate that both were active in the Middle Miocene (13 Ma) [63].

The STDS is well exposed at the southern end of the Yadong–Gulu rift in eastern Himalaya. Here, the shear zone appears to be cut orthogonally by the north–south-trending rift. This configuration presents an exceptional opportunity to better understand the development and kinematic interrelation between these distinct extensional structures. Previous studies of the tectonic evolution of the Yadong area have mainly focused on the evolution of the STDS or NSTRs separately [50,75,81–83], without much attention being paid to the genetic connections and potential interactions between the two structures. The fission track thermochronology system exhibits a low closure temperature. Fission track ages record the time of rock cooling during the exhumation of deep-seated rocks. In the case of apatite during rapid cooling, the closure temperature is 110 ± 10 °C and, for zircon, it is 205 ± 18 °C [84,85]. Consequently, this method is highly sensitive to erosional or tectonic exhumation events in the shallow crust [86,87]. This paper presents new apatite and zircon fission track thermochronology from a sub-vertical profile in the footwall of these two structures in the Yadong area. Pecube thermokinematic modeling of this and previously published data allows the identification of regional tectonic evolution history, providing insights into the inter-relation between the north–south and east–west extensions in a region critical to understanding the evolutionary shift of Himalayan extensional structures.

2. Geological Setting

2.1. Himalayan Orogenic Belt

The Himalayan orogen contains four large orogenic-parallel faults that run from west to east and slice the Himalaya into a series of orogenic wedges: the STDS, Main Central Thrust (MCT), Main Boundary Thrust (MBT), and Main Frontal Thrust (MFT) (Figure 2A) [88]. The STDS marks the structural boundary between the granulite-facies schists, gneisses, migmatites, and calc-silicates of the GHS and the overlying low-grade metamorphic to unmetamorphosed Cambrian to Eocene THS [11,89]. The MCT forms the base of the GHS, as well as the top boundary of the Precambrian clastic sediments and metasedimentary rocks of the Lesser Himalayan Sequence (LHS) [90,91]. The MBT is the boundary demarcation of the LHS and Sub-Himalaya. The Sub-Himalaya, also known as the Siwalik Group, comprises Cenozoic foreland sediments. To the south, the MFT is the southern border of the Himalayan orogen [4,92].

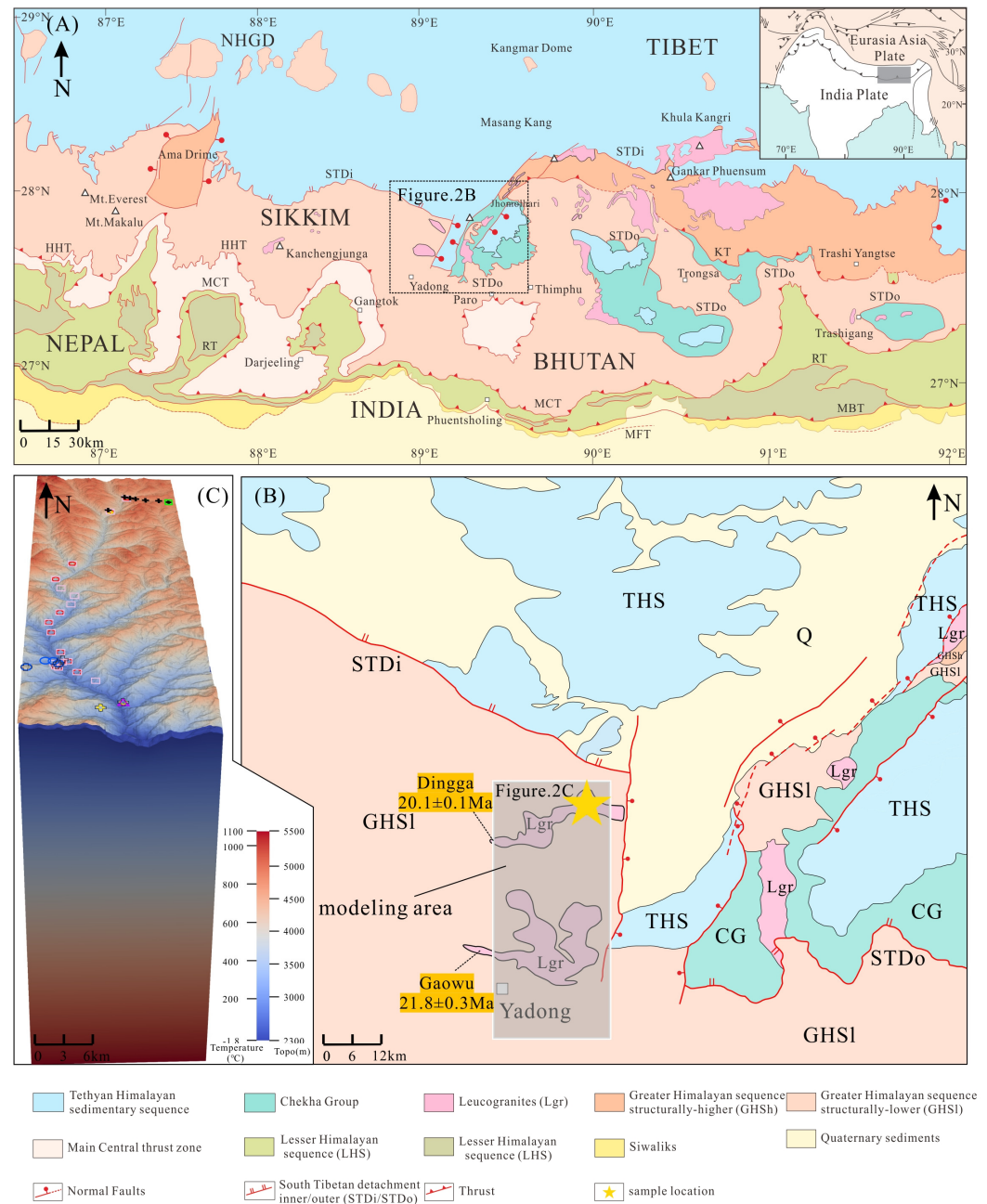


Figure 2. (A) Geological map of the eastern Himalaya (modified from Kellett et al. [64] and reference therein). The black dashed box represents the area contained in Figure 2B. (B) Simplified geological map of Yadong region (Long et al. [93] and reference therein). THS = Tethyan Himalayan sedimentary sequence, GHS(l/h) = Greater Himalayan sequence (structurally lower/higher level), STD_i = inner STD system, STD_o = outer STD system [94]. The black text within the orange box represents the name of the pluton, along with its crystallization age (Ma) [83]. The gray shadow coverage area is the thermokinematic numerical modeling area of the Pecube. (C) Model setup for Pecube modeling of this work. The various symbols on the top of the topography represent thermochronological ages that have been used as model inputs. Our AFT data are marked by a black solid cross, ZFT data are marked by a green square, referenced AFT data are marked by a black hollow cross, referenced AHe data are marked by a red pentagon, referenced ZFT data are marked by a pink square, referenced ZHe data are marked by a blue circle, referenced ZFT data are marked by a pink square, and purple triangle and yellow diamond represent ⁴⁰Ar/³⁹Ar ages of muscovite and biotite, respectively [81–83].

2.2. Structure and Deformation of the STDS

The STDS is a suite of low-angle, north-dipping, and normal-sense-of-motion subparallel faults [4,73]. The motion along the primary trace of the STDS consists of ductile shear and, later, ductile-brittle to brittle slip [4,89]. The shear zone can be identified along the entire trace of the STDS, while brittle faults are only locally observed, such as the Everest Massif [95]. The ductile shear zone, which is at a lower structural level, is typically a few km thick and developed within the uppermost part of the GHS. An upright metamorphic field gradient from lower greenschist facies (250–450 °C) to upper amphibolite facies (650–750 °C) at the base has been identified within the ductile shear zone [60,67,94,96–99]. The rocks in the shear zone generally display retrograde P–T–t paths [67].

The structurally higher part, the ductile-brittle to brittle fault, comprises several discrete normal faults that separate the metamorphosed GHS from the unmetamorphosed or low-grade Paleozoic and Mesozoic sedimentary THS [100,101]. The microstructural characteristics of the fault zone rocks indicate low-temperature deformational conditions (~300 °C), while pressure plays a major role in the deformation [73].

Along the length of the STDS, a set of leucogranites was emplaced during the Oligocene–Miocene. Their formation is thought to be linked to the migmatitic partial melting of the middle crust during the India–Asia collision process or post-collisional stage [102,103]. The dating of pre-, syn-, and post-tectonic leucogranite bodies within the shear zone and determining the exhumation ages of the GHS are major methods to constrain the timing and evolution of motion along the STD [64,75,95,104].

2.3. Geological Characteristics of the NSTRs

Many north–south trending faults have developed within the Tibetan Plateau, several extending northward into the Qiangtang terrane [14,26,38,45]. They appear to have played a vital role in accommodating the east–west extension of the Tibetan Plateau. They represent the latest tectonic deformation associated with the subducting Indian slab and are the most active tectonic system in the plateau at the present time [88,105]. The spacing between rifts displays a distinctive pattern of being narrower in the western portion and broader in the eastern region. The age of NSTRs generally falls within the age range of between 19 and 3 Ma [30,31,53]; certain rifts exhibit an initial onset time predating 20 Ma [15]. There are variations in the initiation ages among different rifts. Overall, the initial age decreases progressively from west to east [53]. The presence of ultrapotassic rocks in the Plateau region, primarily exposed along rifts, suggests a potential inherent genetic connection between them [106–108].

2.4. Yadong Regional Structural Setting

Yadong is located in the eastern part of the Himalayan orogenic belt, bounded by STDS, with THS in the north and GHS in the south (Figure 2A,B). The THS is composed of Ordovician to Cretaceous carbonates and clastic sediments that, in some places, have undergone low-grade metamorphism and weak deformation [101]. The GHS is composed of paragneiss, marble, and calc-silicate rocks that are highly metamorphosed and deformed. Zircon U–Pb ages of 17 Ma from the Zherger-La HP granulite likely records the initiation of extrusion and exhumation of the GHS [81,109]. Along the strike of the STDS, there are several leucogranite dykes and sills and two large plutons (Dingga and Gaowu). Dong et al. [38] reported Early Miocene zircon U–Pb ages of 20–22 Ma for the magmatism.

To the west, the STDS extends into northern Sikkim. Kellett et al. [64] determined that the Sikkim STDS was active between 23.6 and 13 Ma. The STDS continues eastward to northern Bhutan and splits into two branches. The northern segment, closer to the orogenic front, is considered to be the inner STDS (STD_i), and the southern segment is regarded as the outer STDS (STD_o) [66]. The former separates the THS from the metasedimentary Chekha group (local name in Bhutan), while the STD_o separates the amphibolite and granulite facies (at a structurally higher level, the GHSh) from the metasedimentary unit (at a structurally lower level, the GHS_l) ([93] and references therein). Cooper et al. [12]

extracted geochronological data from leucogranite and metasedimentary rocks collected in the footwall and demonstrated that deformation in Bhutan's STDS persisted at least until 14 Ma, and the N–S fault as well as the STDS underwent protracted and overlapping histories of deformation.

The Yadong–Gulu rift stretches over 500 km and is one of the longest NSTRs. The northern end extends to the Lhasa terrane, and the southern end passes through the Yarlung Zangbo belt and THS into the Himalayan terrane. The southernmost segment, also known as the Yadong fault, cuts the STDS, offsetting it in a left-lateral sense by at least 70 km [81].

3. Methods

Seven granite samples were collected from the Dingga pluton. Six samples were collected along a sub-vertical transect over approximately 600 m (Figure 3A,B). The limited horizontal distance between samples is an attempt to minimize the influence of the wavelength of the topography on age–elevation relationship results.

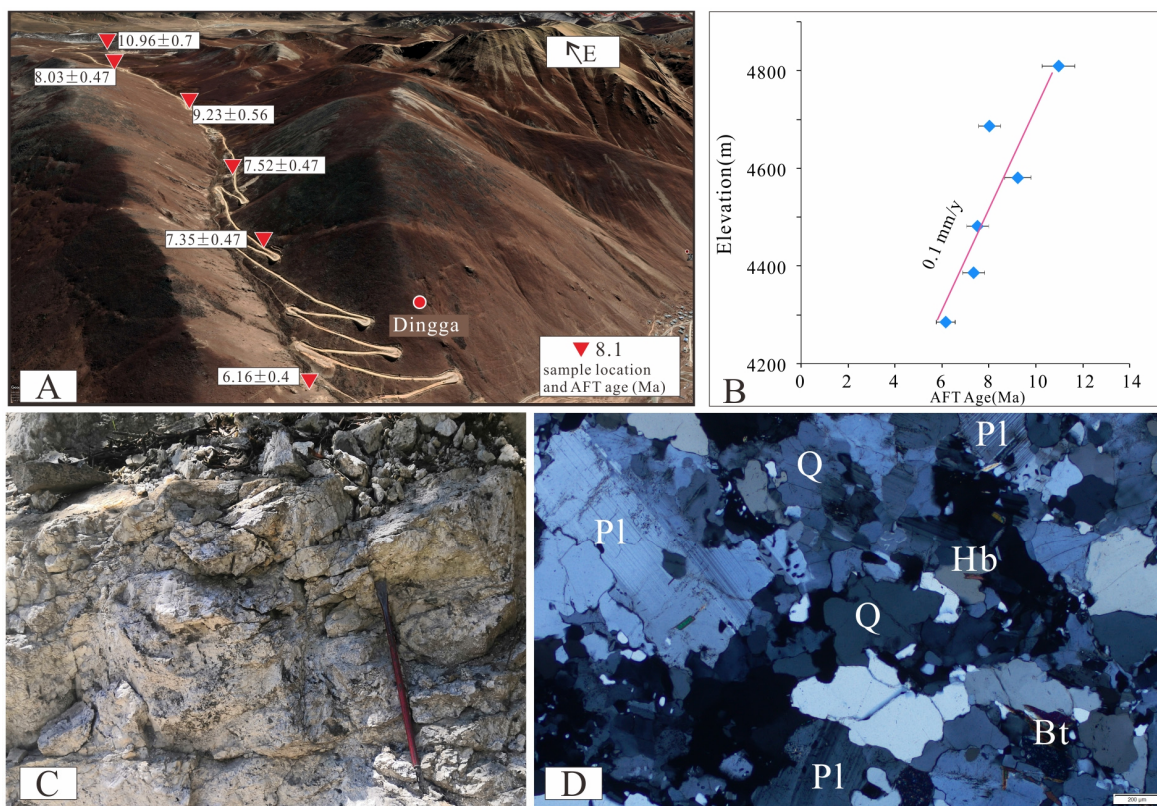


Figure 3. (A) Google Earth image of the sampling profile; the sampling location and AFT ages are marked as red inverted triangles and white boxes. (B) Age–elevation plots of the sampling profile. The blue dots represent the age and elevation of each sample, black horizontal lines indicate the error, and the slope represents the average exhumation rate. The plots showing that the exhumation rate was 0.1 km/Myr between 11 and 6 Ma. (C) Field outcrops of the Dingga pluton. (D) Thin section photographs of Dingga granite. “Pl” represents plagioclase; “Q” represents quartz; “Hb” represents hornblende; “Bt” represents biotite.

The samples are dark gray, characterized by a medium-grained texture and blocky structure (Figure 3C). They are composed of 40–50 vol.% quartz, 30–35 vol.% plagioclase, 10–15 vol.% biotite, 5 vol.% hornblende, and trace amounts of accessory minerals. Biotite and hornblende display chloritization (Figure 3D).

The samples were crushed, and apatite and zircon grains were concentrated using conventional heavy liquid and magnetic separation methods. For fission track analysis, grains were embedded in epoxy resin (apatite) and FEP Teflon (zircon), followed by grind-

ing and polishing. Zircon crystals were etched for 20–35 h with NaOH/KOH (=1:1) eutectic etchant at 210 °C, while apatite crystals were etched in 5.5% HNO₃ for 20 s at 21 °C. Thin, low-uranium muscovites were used as external detectors and packed together with sample grain mounts and CN2, as well as CN5 uranium dosimeter glass, which was then irradiated in a well-thermalized hot-neutron nuclear reactor [110]. Post-irradiation, the muscovite external detectors were separated and etched in 40% HF for 20 min at 25 °C to reveal induced fission tracks. Track densities for both spontaneous and induced fission track populations were assessed with a dry objective at 100× magnification. Fission track ages (FTAs) were determined using the International Union of Geological Sciences (IUGS)-recommended Zeta calibration approach, with the Zeta values derived from repeated measurements of standard apatites [111,112].

In order to reconstruct the tectonic and exhumation, we have used Pecube (V4.2.1) [113], a software that is designed to interpret thermochronological data by solving the heat equation in 3D in the crust (Supplementary for detailed description of Pecube).

4. Results

AFT ages from the seven samples are in the range of 5.7–11.0 Ma (detailed in Figure 4, Table 1). XTK61, the highest sample, displays the oldest age ($\sim 10.96 \pm 0.7$ Ma), with a confined mean track length (MTL) of 12.5 ± 2.1 μm . Samples XTK-62 and XTK-63 yielded AFT ages of 8.03 ± 0.47 and 9.23 ± 0.56 Ma, with slightly longer MTL values of 12.9 ± 1.9 and 12.7 ± 1.4 μm , respectively. The other three samples of sub-vertical transect (XTK64, XTK65, XTK-PL2) yielded ages between 7.52 ± 0.47 Ma and 6.16 ± 0.47 Ma. The sample from the lowest elevation yields the youngest age of 5.68 ± 0.37 Ma. Sample XTK-61 yielded a ZFT age of 13.57 ± 0.61 Ma and did not pass the χ^2 test.

Table 1. Summary information of collected samples.

Sample No.	Longitude (°)	Latitude (°)	Elevation (m)	N	ρ_s ($10^5/\text{cm}^2$) (Ns)	ρ_i ($10^5/\text{cm}^2$) (Ni)	ρ_d ($10^5/\text{cm}^2$) (N)	P(χ^2) (%)	Central Age (Ma) ($\pm 1\sigma$)	MTL (μm)
<i>AFT result</i>										
XTK61	89.055	27.784	4809	35	3.056 (2041)	78.109 (52,173)	14.721 (6630)	0	10.96 ± 0.7	12.5 ± 2.1
XTK62	89.042	27.787	4686	37	1.061 (842)	40.228 (31,912)	15.615 (6630)	25	8.03 ± 0.47	12.9 ± 1.9
XTK63	89.025	27.788	4581	35	1.517 (797)	52.974 (27,828)	16.509 (6630)	23	9.23 ± 0.56	12.7 ± 1.4
XTK64	89.012	27.791	4482	34	1.187 (679)	37.476 (21,444)	12.933 (6630)	37	7.52 ± 0.47	12.0 ± 2.1
XTK65	89.004	27.793	4386	35	1.147 (1067)	41.445 (38,557)	13.827 (6630)	0	7.35 ± 0.47	11.6 ± 2
XTK-PL2	88.997	27.795	4285	35	1.193 (867)	58.429 (42,445)	15.615 (6630)	1	6.16 ± 0.4	13.4 ± 2
XTK-KB1	88.974	27.757	3855	35	0.619 (478)	31.321 (24,200)	14.721 (6630)	100	5.68 ± 0.37	12.7 ± 1.8
<i>ZFT result</i>										
XTK-61	89.055	27.784	4809	36	31.389 (2777)	107.517 (9512)	10.56 (6844)	0	13.57 ± 0.61	

All samples were dated using the external detector method. The AFT and ZFT ages were evaluated by the RadialPlotter [114].

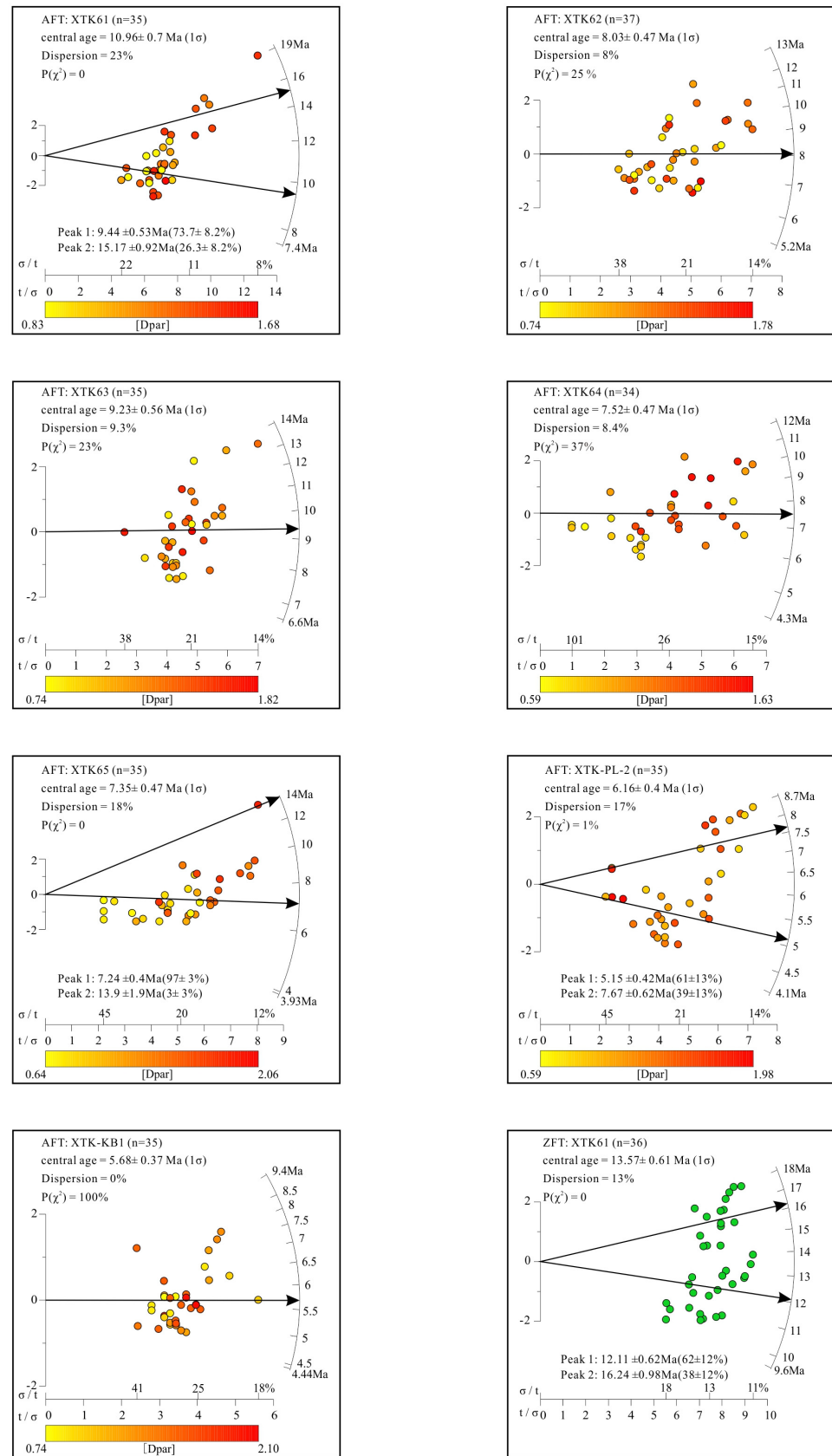


Figure 4. Individual grain ages for samples were assessed using RadialPlotter [114]. The radial plot illustrates the single –grain age through the degree of rotation along the curved axis, with analytical uncertainty represented by the distance from the curved axis. Component ages are depicted as radiating lines, and the values of Dpar are also presented in the radial plot.

The track length distributions of samples are unimodal, with standard deviations between 1.4 and 2.1 μm , and exhibit a negative skewness, with mean track lengths of 11.6 and 13.4 μm (Figure 5, Table 1), indicating that the samples have not been disturbed thermally since cooling [115]. The six samples from the sub-vertical transect show a positive age-elevation relationship (Figure 3B). Assuming that this reflects cooling through the AFT closure temperature, they yield an average exhumation rate of ~ 0.1 km/Myr between 11 and 6.2 Ma.

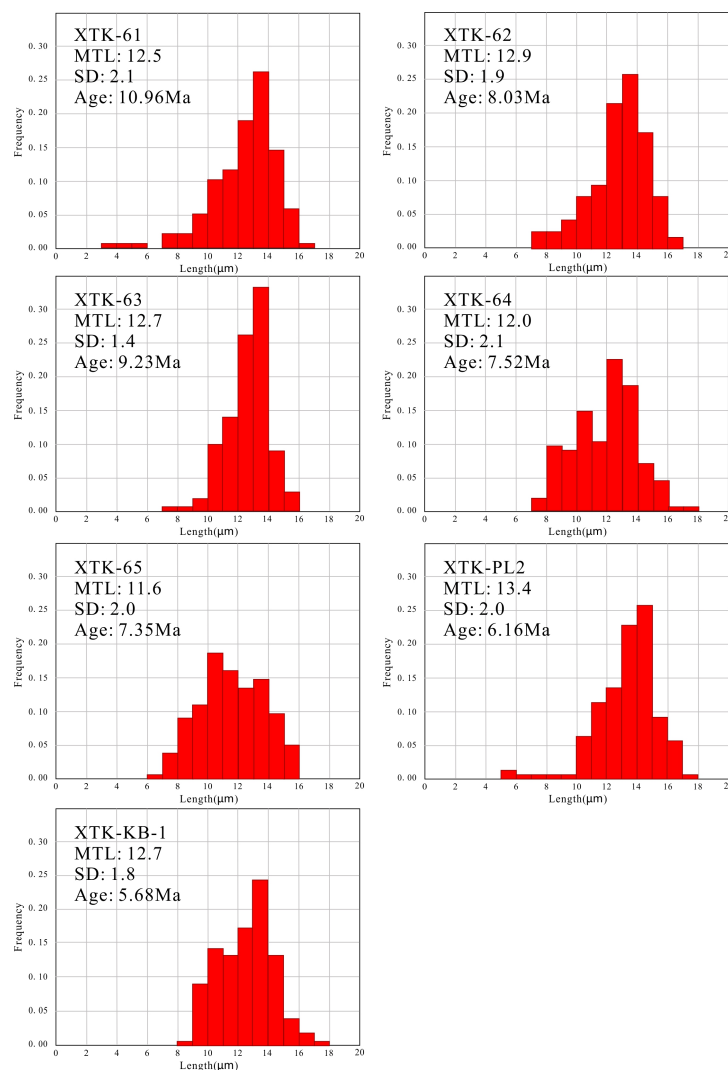


Figure 5. Fission track length distributions of samples. MTL represents mean track length; SD represents the standard deviation of the confined fission track lengths.

It should be noted that the AFT age of XTK-61, XTK-65, and XTK-PL2, and the ZFT age of XTK61 do not pass the χ^2 test, suggesting multiple age groups (Figure 4). This phenomenon has also been observed in previous investigations of Himalayan granites [82,116,117]. This may be attributed to the intricate genesis of the Himalayan leucogranite [118,119], coupled with the presence of hydrothermal alteration or mineral inclusions. This would result in differences in chemical composition, leading to inconsistent annealing properties among some grains. However, given that only a small number of the 35 grains in each sample are affected, the overall impact on the age is small. Consequently, we have opted to retain the data that do not pass the chi-square test.

5. Thermal History and Thermokinematic Numerical Modeling

5.1. Thermal History from HeFTy Modeling

The thermal histories have been modeled using the software HeFTy (V2.1.7) [84]. AFT data were simulated using the Ketchum et al. [120] multi-kinetic annealing model, employing Dpar as a kinetic parameter. We selected two samples from the top and bottom of the elevation profile for modeling and compared them with samples from Sikkim [64], which is located in the immediate footwall of the Inner STDS and the southern part of Yadong County [83]. The results of this modeling indicate a rapid cooling around 12–14 Ma, followed by a slower cooling rate in the middle to late Miocene, which suggests a quite stable tectonic setting during this time. Towards the end of the Miocene, there is evidence of another phase of rapid cooling, which is represented by grey stripes in Figure 6a,b.

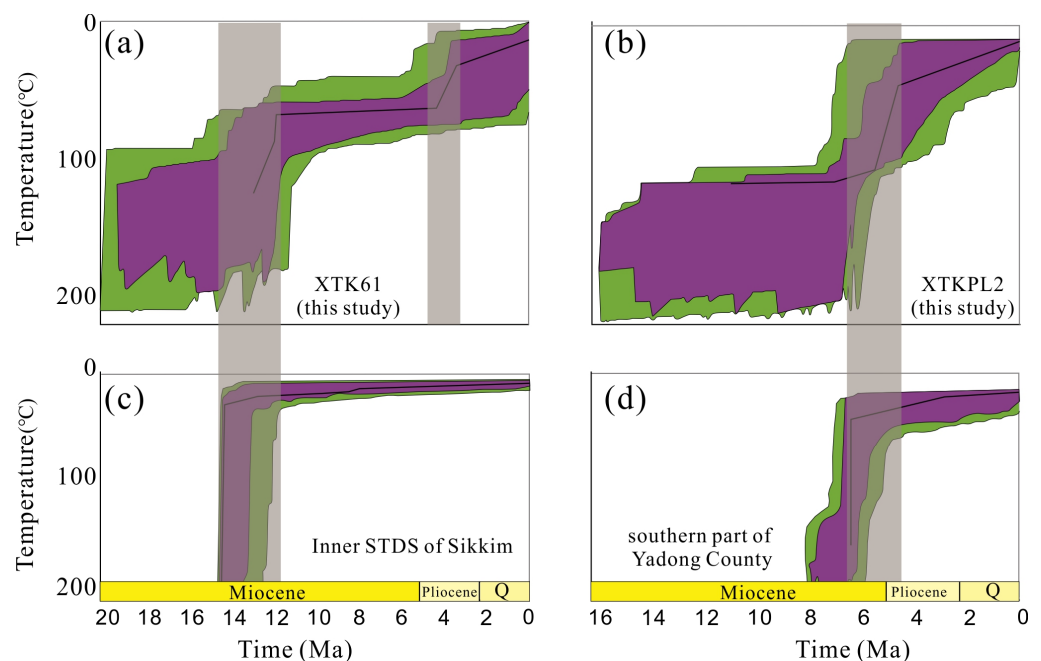


Figure 6. Representative HeFTy models for samples from (a) top and (b) bottom of the sub-vertical transect, (c) from the immediate footwall of the Inner STDS of Sikkim [64], and (d) from the southern part of Yadong County [83]. The gray bands indicate periods of rapid cooling. Purple envelopes represent ‘good’ thermal paths (goodness of fit (GOF) > 0.5), while green envelopes represent ‘acceptable’ thermal paths (GOF > 0.05). The optimal thermal path for each sample is depicted by a black line.

5.2. Pecube Model Setup

In order to model the regional cooling history, we have selected a domain (56×18 km) around the Dingga and Gaowu plutons that extends north to near the main trace of STDS and in the footwall of the STDS, as well as the Yadong fault (Figure 2C). We use a digital elevation model (DEM) of the present-day surface as the topography of the model. Recent research conducted in the Yadong region has revealed that while the ductile deformation of STDS ended around 20 Ma [75], brittle movement persisted after 16 Ma [83], and the area experienced rapid exhumation-related cooling in the Middle Miocene [81,82]. Thirty-five sets of thermochronological ages are incorporated in the Pecube model which is aimed at determining how exhumation, geothermal gradient, and topography have changed—these ages include apatite (U-Th)/He (AHe), AFT, zircon (U-Th)/He (ZHe), ZFT, biotite $^{40}\text{Ar}/^{39}\text{Ar}$ (BAr), and muscovite $^{40}\text{Ar}/^{39}\text{Ar}$ (MAr) (for details, the data are listed in Supplementary Table S2). Given that the oldest BAr age is 15 Ma and the Pecube model cannot currently simulate ductile fault deformation, we set 16 Ma as the starting time of the model.

Twenty-five inversion models were run in the Advanced Computing East China Subcenter. Each inversion model contained 10,000–50,000 forward modeling times. We have selected the five inversion models that are most consistent with the geological constraints.

The oldest and youngest AFT ages from the sub-vertical profile are 11 and 6.2 Ma, respectively, and yield an average exhumation rate of ~0.1 km/Myr. Therefore, in the model, we regard 11 and 6.2 Ma as key times when exhumation rates changed. In the models below, we vary the number of phases of exhumation between 3 and 5 (Figure S1). Table 2 shows the default thermal and flexural parameter settings in our mode. Table 3 shows the inversion results of Pecube for the different scenarios. We will explicate the five models.

Table 2. Default thermal parameter input Pecube.

Thermal Parameters	Value	Reference
Crustal density (kg/m ³)	2700	[121]
Mantle density (kg/m ³)	3200	[121]
Young's modulus (Pa)	1.1011	[121]
Poisson ratio	0.25	[121]
Equivalent elastic thickness(km)	22.8	[122]
sea level temperature (°C)	15	[123]
model thickness (km)	35	[124]
Thermal diffusivity (km ² /Myr)	25	[121]
Atmospheric lapse rate (°C/km)	6	[125]
Radiogenic heat production (°C/Myr)	9	[121]

Table 3. Inversion results of Pecube for the different scenarios.

Model Name	YD01	YD02	YD03	YD04	YD05
Best misfit	4.99	4.06	4.91	4.06	4.18
T _b (°C)	947 (900:1200)	904 (900:1200)	1125 (900:1200)	1077 (900:1200)	1038 (900:1200)
Topographic evolution	nil	nil	nil	nil	0.1/5
Exhumation stage	3	4	4	5	5
Stage 1 (Ma)	16–11	16–11	16–12.1	16–12.3	16–15.1
E 1 (km/Myr)	1.46	1.25	0.98	1.61	3.77
Stage 2 (Ma)	11–6.2	11–6.2	12.1–11	12.3–11	15.1–11
E 2 (km/Myr)	0.47	0.49	0.33	1.79	0.89
Stage 3 (Ma)	6.2–0	6.2–5	11–6.2	11–6.2	11–6.2
E 3 (km/Myr)	0.6	2.9	0.34	0.17	0.39
Stage 4 (Ma)	nil	5–0	6.2–0	6.2–4.7	6.2–5.7
E 4 (km/Myr)	nil	0.29	0.1	2.52	1.77
Stage5 (Ma)	nil	nil	nil	4.7–0	5.7–0
E 5 (km/Myr)	nil	nil	nil	0.28	1.11

T_b represents the temperature at the bottom of the model; the range of temperature is denoted by values in brackets, while the lowest misfit values for models are highlighted in bold. Within the topographic evolution line, the topography amplification is denoted by the number preceding the semicolon, while the offset value is indicated by the number following the semicolon. The variables Stage and E represent distinct exhumation stages along with their corresponding exhumation rates.

5.3. Modeling Results

5.3.1. YD01 Scenario

In this model, we assume that the region experienced three exhumation stages (16–11 Ma, 11–6.2 Ma, and 6.2 to the present day) and steady-state topography. The numerical simulation results show that the exhumation rate is 1.46 km/Myr from 16 to 11 Ma, a lower cooling rate (0.47 km/Myr) from 11 to 6.2 Ma that is followed by rapid exhumation at a rate of 0.6 km/Myr since 6.2 Ma (Figure S2). The model results also generate the temperature at the bottom of the model (947 °C), which implies a geothermal gradient of 27 °C/km.

Scatter plots for the inversion model show that the parameters do not converge well to the lowest misfit, although 1D-PPDFs reveal that the parameters are well resolved. Furthermore, we note that while the exhumation rate from 11 to 6.2 Ma (0.47 km/Myr) is not particularly fast, it is significantly higher than the rate (0.1 km/Myr) determined from our elevation profile data for the middle–late Miocene.

5.3.2. Scenario YD02

In this inversion, we assume that there have been four distinct exhumation periods, and the topography has remained in a steady state. Compared with YD01, 6.2–0 Ma is separated by an uncertain transition time into two stages, and the remaining stages are unchanged. We ran 10,000 models (60 iterations of 150 models, with 1000 cells resampled).

The model gives the lowest misfit of 4.06, and the misfit scatterplots and the posterior PPDFs of the parameter values demonstrate that most of the input-free parameters of this inversion are rather well bounded. The best-fit model requires that the exhumation rate is 1.25 km/Myr between 16 and 11 Ma. A cooling rate of 0.49 km/Myr was also obtained for the middle to late Miocene. The rate of exhumation from 5 Ma to the present is 0.29 km/Myr, which comes after a brief period of rapid exhumation (2.9 km/Myr from 6.2 to 5 Ma). According to the model, the temperature at the base is estimated to be 904 °C; consequently, the geothermal gradient has been 26 °C/km.

Figure S2 shows that the bottom temperature derived by this model is very close to the minimum border of the specified parameter range (900–1200 °C). It is possible that we will obtain a lower geothermal gradient if we expand the bottom temperature range. Given the simulated geothermal gradient of only 26 °C/km at the plateau region, the sustained decline in bottom temperature unequivocally contravenes geological principles. For the same reason, the value of the short-term rapid exhumation at the end of the Miocene is also close to the parameter boundary, and the scatter diagram shows that it is not well constrained.

5.3.3. YD03 Scenario

YD03 has modeled four distinct exhumation stages. The new transition time is within 16–11 Ma, unlike YD02. The best-fit model indicates that the exhumation rate in the study area is 0.98 km/Myr between 16 and 12.1 Ma and 0.33 km/Myr within the next 1 Myr. Exhumation is at a rate of 0.34 km/Myr between 11 and 6.2 Ma, and it was relatively slow, at barely 0.1 km/Myr since the end of the Miocene. In this model, the temperature at 35 km is 1125 °C, which means that the average geothermal gradient was 32 °C/km.

While the 10,000 model runs have yielded a good misfit value (4.91), it is clear from the misfit scatterplots and the posterior PPDFs of parameter values that the model is not perfect (Figure S2). The free parameters, such as the temperature at the bottom of the model, the transition time of the exhumation rate, and the exhumation rate of each phase, are not well resolved, and the results of the optimal misfit parameters are beyond the convergence window.

5.3.4. YD04 Scenario

In this inversion, we assume that the topography has not changed and that there have been five phases of exhumation. Ages 16–11 Ma and 6.2–0 Ma are separated by an uncertain transition time into two stages, respectively. This model achieved the lowest misfit of 4.06 based on 51,000 forward runs. According to the best-fit results, the initial exhumation rate reached 1.61 km/Myr, followed by a transition at 12.3 Ma that caused an acceleration in cooling to 1.81 km/Myr until 11 Ma. Between 11 Ma and 6.2 Ma, the exhumation rate was 0.17 km/Myr, which is consistent with our age–elevation relationship. Following a period of rapid exhumation between 6.2 and 4.7 Ma, at a rate of 2.5 km/Myr, the exhumation rate remained relatively stable at 0.28 km/Myr from the early Pliocene. The posterior PPDFs of the parameter values and the misfit scatterplots demonstrate that the parameters utilized in this scenario are highly constrained (Figure 7).

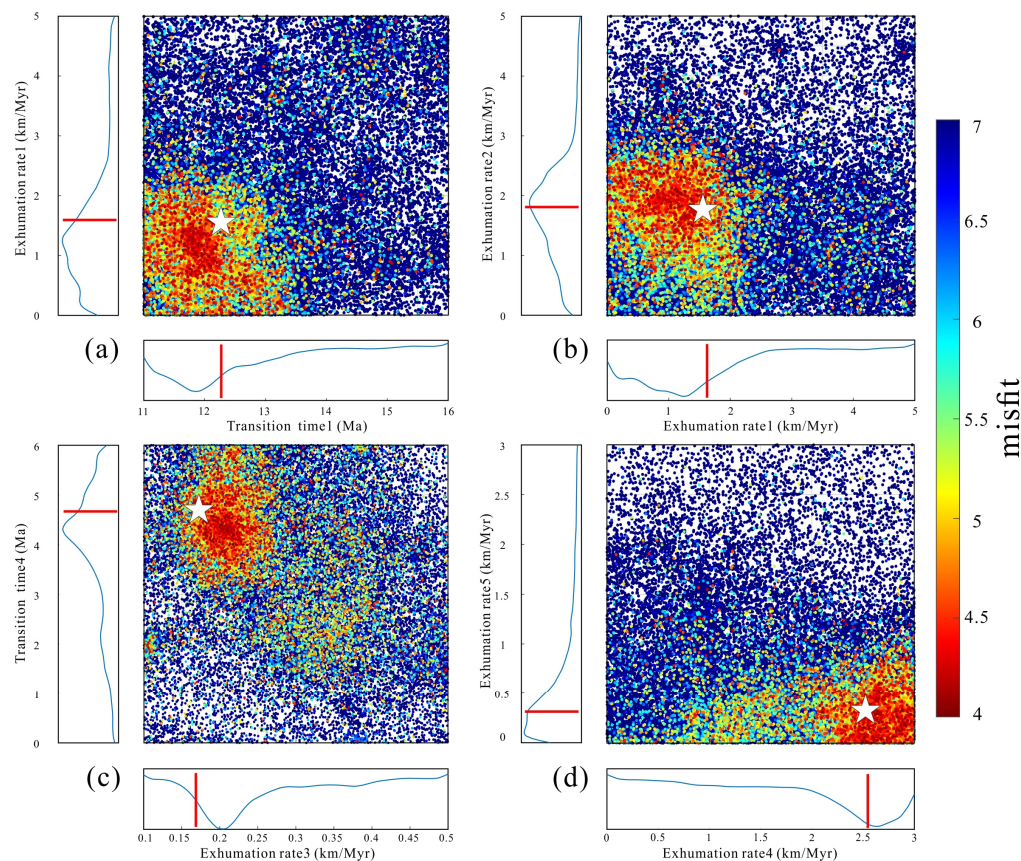


Figure 7. Scatterplots of the Pecube inversion results for model YD04. The white star denotes the optimal solution obtained from the analysis. The red lines indicate parameter values for the lowest misfit forward model. (a) Transition time 1 (between the first and second exhumation phases) versus the exhumation rate during the first phase. (b) Exhumation rate during the first phase versus the exhumation rate during the second phase. (c) Exhumation rate during the third phase versus transition time 4 (between the fourth and last exhumation phases). (d) Exhumation rate during the fourth phase versus the exhumation rate during the last stage.

5.3.5. YD05 Scenario

To investigate the impact of incision on the cooling history, building upon model YD04, model YD05 started with a plateau at 5000 m and imposed 10% of the present-day relief at the beginning of the model and linear evolution toward the present topography. This kind of proto-plateau scenario has been shown in the study of Mount Everest [124]. Because there is only one river in the study area, we assume that the increase in the relief results from preferential fluvial erosion; in other words, valley bottoms decrease while ridges maintain a fixed elevation in relation to an external reference frame.

This inversion includes 10,000 forward models, and the minimum obtained misfit is 4.18. The best-fit results show that the exhumation rate in the Yadong area is 3.77 km/Myr between 16 and 15 Ma, and over the next 4 Myr, it is 0.89 km/Myr. The exhumation rate between 11 and 6.2 Ma is 0.39 km/Myr, which is followed by a phase of swift exhumation at 1.77 km/Myr between 6.2 and 5.7 Ma that slowed to 1.11 km/Myr until the present. The posterior PPDFs and the misfit scatterplots (Figure S2) demonstrate that the free parameters in this scenario are not well limited, although misfit values are close to those of the earlier models.

6. Discussion

The best-fit cooling history (YD04) implies that the region underwent five distinct stages of exhumation (Figure 8). Figure 9 shows the agreement between the observed

and predicted ages of the best-fit model, with the majority of the samples displaying consistency. Only a minor proportion of older samples exhibit variances, which can possibly be attributed to the limited size of the corresponding age bracket.

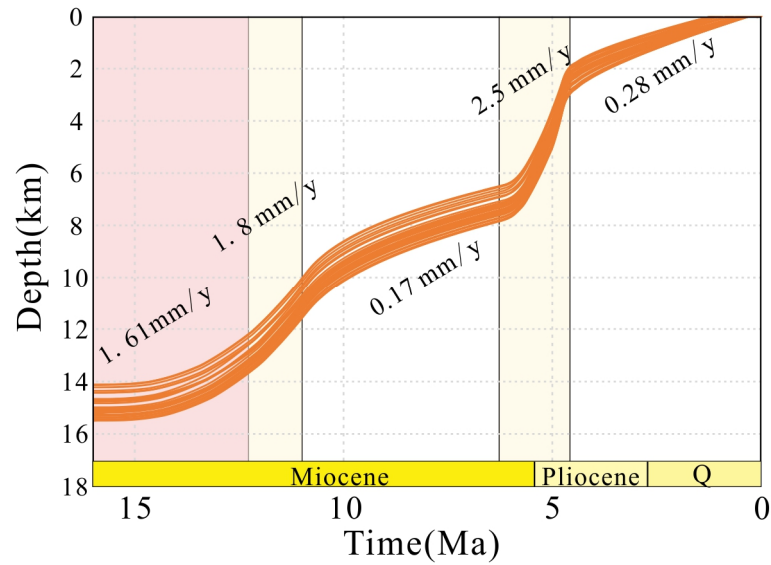


Figure 8. Time-depth plot depicting the evolution of the Yadong region since 16 Ma based on YD04 modeling results. Each orange line represents a sample (each sample information and reference has been listed in the Supplementary Table S2), and depth is calculated based on the simulated geothermal gradient (30.8 °C/km).

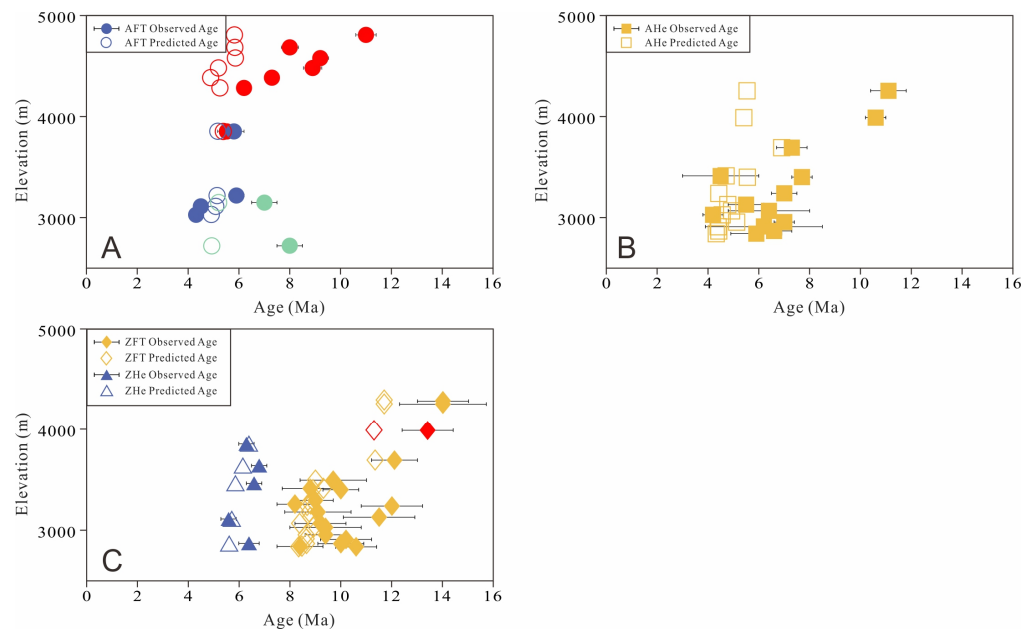


Figure 9. Age–elevation profiles of observed and predicted ages for YD04. (A) Observed AFT ages and predicted ages. (B) Observed AHe ages and predicted ages. (C) Observed/predicted ZFT and ZHe ages, respectively. Empty symbols represent predicted ages, while the corresponding solid symbols represent measured ages. Red symbols represent data from this study, light green symbols are from [81], yellow symbols are from [82], and blue symbols are from [83]. Each sample information and reference has been listed in the Supplementary Table S2.

The incorporation of topography changes in model YD05 reveals that the greatest difference in elevation between the ridges and valleys was approximately 3.2 km within

the last 16 million years, equating to an erosion rate of 0.2 km/Myr. However, Valla et al. [123] demonstrated that for topographic changes to be registered by low-temperature thermometry, growth rates need to be 2–3 times greater than the background exhumation rate. Despite accounting for topographic evolution due to river erosion, our inversion results did not indicate such a low exhumation rate, revealing that topographic changes are insufficient to influence our findings.

6.1. New Constraints on the Movement of STDS

The integrated thermal histories show that the region experienced a pulse of rapid exhumation between 16 and 12.3 Ma at a rate of 1.61 km/Myr (i.e., 1.61 mm/y) and a slowing of exhumation rate to 0.17 km/Myr since 11 Ma. Because of the region located in the footwall wall of STDS, the movement of the STDS will unavoidably result in the exhumation-related cooling of the footwall. Previous studies have shown that the ductile shear of the STDS in the Yadong region terminated at approximately 20 Ma [75], but the brittle slip associated with it lasted to at least 14 Ma [12,65], possibly continuing until 11 Ma [83]. Our results refine these findings, confirming that the motion along the STDS at least continued until after 12.3 Ma and ceased no later than 11 Ma.

Recently, it has been demonstrated that the movement of STDS has been regionally diachronous. Ductile shearing of the STDS came to a halt in the Everest region at 15–13 Ma [95,126–128]. In the Sa'er region, to the east of Everest, the most recent ductile deformation of the STDS occurred between 14.2 and 13.6 Ma [64]. Kellett et al. [64] also used the largely undeformed leucogranites to determine that the most recent ductile activity of the Sikkim STDS occurred before 13 Ma. The latest ductile movement of the STDS in NW Bhutan occurred between 11 and 10 Ma [66,69–72]. The cessation time of brittle slip has also varied. Schultz et al. [129] performed a low-temperature thermochronology study to constrain the brittle slip cessation time of the STDS in the Everest area and obtained an age of 13 Ma. Previous studies have shown that the brittle activity of the STDS in the Dinggye area persisted possibly until 11 Ma [61,63]. In addition, the different segments across the strike appear to present local diachroneity. The brittle–ductile transition in a branch of the STDS, which is preserved in Bhutan klippen, occurred during 20–13 Ma, while the ductile shear of the STDS in the main trace continued until at least 11 Ma ([89] and references therein).

The fresh data and interpretations offered here, together with data that have already been published, show that the cessation of STDS has a temporal progression, whether it is the early ductile activity or the later brittle sliding. Webb et al. [130] used a comprehensive review of data to demonstrate that the cessation of STDS appears to be diachronous along the Himalayas, from early in the western Himalaya (24–20 Ma) to the easterncentral Himalaya (13–11 Ma) for a duration of approximately 13 My, and there is a general tendency towards becoming younger from west to east. The age constraints from Sikkim (ca. 13 Ma)-Yadong (12.3–11 Ma)-Bhutan (11–10 Ma) align with this trend. Certainly, due to constraints related to sampling locations, sample types, and experimental methods, the true significance represented by different ages may vary. However, they still provide valuable references for subsequent research on the STDS.

6.2. New Constraints on the Movement of NSTRs

The results of the inversion procedure suggest that the region experienced a short-lived exhumation pulse between 12.3 and 11 Ma, which coincides with the end of the brittle slip of the STDS. It appears unlikely that STDS would affect the exhumation rate to cause such an increase. Given that the study area is situated at the footwall of the southern end of the Yadong rift, we assume that the force driving exhumation during this stage came from the east–west extension. This age constraint for the initiation of the Yadong fault aligns with previous age estimates in the region. Based on K–Ar dating and paleomagnetic analysis of the sediments in the adjacent sedimentary basins, Antolín et al. [49] proposed that the Yadong normal fault initially formed at 13 Ma. Cooper et al. [12] employed zircon

U-Pb dating of leucogranite veins that cross-cut the STDS and NSTRs and proposed that the east–west extension occurred at 14 Ma. U-Pb monazite ages from the Khula Kangri granite, Tibet-Bhutan frontier show that the onset of the Yadong-Gulu rift is probably younger than 10 Ma [46]. Studies of the Pali Basin in northeastern Yadong indicate that the Yadong fault began at ca. 13 Ma [131]. It has recently been shown from low-temperature thermochronology and thermokinematic modeling that the Yadong fault began at 13–11 Ma and had a slip rate of 1 km/Myr [50]. The STDS may have ceased to be active at this stage, and the east–west extension was responsible for the relatively high exhumation rate (~1.8 km/Myr). Another plausible scenario is that at this time, the brittle slip along the STDS was still ongoing, and it, in conjunction with the activity of the Yadong normal fault, collectively resulted in an exhumation rate of 1.8 km/Myr. Considering the initiation age of other rifts, it can be inferred that the initial activity of the rift exhibits a trend of becoming progressively younger from west to east.

It is noteworthy that our results are slightly older than the recent K–Ar ages (9 ± 1 Ma) of illite from fault gouges 70 km to the north [132]. This may be explained by along-strike variation in the activity of the Yadong-Gulu rift, as well as variations in the onset time of faulting among different segments of the rift. Wolff et al. [133], in their study of the Tangra Yumco graben, propose that fault activity propagates northward at a rate of 25 km/Myr. Considering the age difference of ca. 3 Ma and the distance between the two sites, the average propagation rate of the Yadong rift is closely aligned with this value.

From 11 Ma onwards, the Yadong area experienced regional exhumation at a rate of 0.17 km/Myr until 6 Ma, suggesting that both the STDS and Yadong fault activity had ceased. A third pulse of fast exhumation appears to have initiated at ~6.2 Ma and lasted until 4.7 Ma. We assume that the second phase of the normal fault (Figure 10). This is consistent with the paleomagnetic analysis of Pali basin sedimentation by He [131], who proposed that the contraction of the basin during this period is correlated with the activity of neighboring faults.

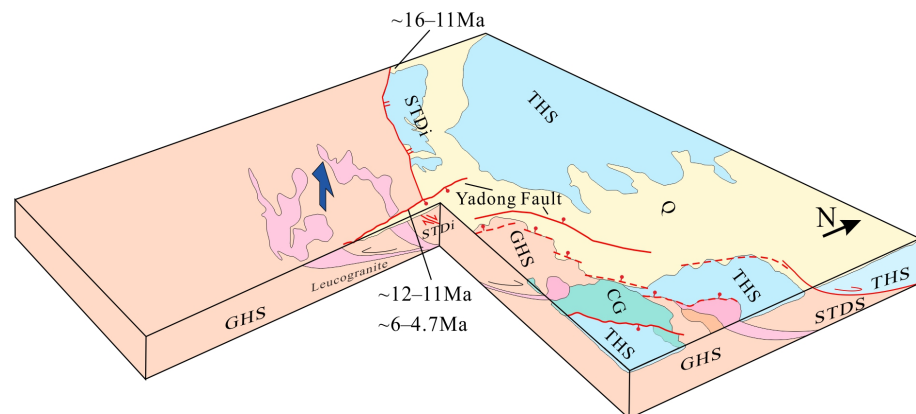


Figure 10. Schematic diagram of extensional tectonic activity in the Yadong area (modified from Kellett et al. [64] and reference therein). Since the middle Miocene (16 Ma), the brittle movement of the STDS continued until at least 12 Ma and probably until ca. 11 Ma. There were two phases of east–west extension: the first occurred from 12–11 Ma, and the second occurred from 6–4.7 Ma. Blue vertical arrows indicate locations of uplift and exhumation. The legend for this figure is identical to that of Figure 2.

A second period of activity has been recognized on several NSTRs. The Kung Co fault initiated at 19 Ma and experienced a second extensional stage at 4 Ma [1,30]. Sundell et al. [21] conducted a low-temperature thermochronological study on the Lunggar rift. The results showed that the rift was formed prior to 10 Ma, and the extensional rate of the rift was 1 km/Myr, while the rift was rapidly extended at a rate of 4–10 km/Myr at 5–2 Ma. In addition, Sundell et al. [21] believe that two-stage activities are also commonly found in other rifts in southern Tibet. Although not all rifts have currently been found to exhibit

two-stage movement, the second phase of activity could be masked by factors such as sampling locations and experimental methods.

A significant quantity of adakite and ultrapotassic rocks is recognized in the Tibet Plateau. The ages of these rocks (8–25 Ma) are not only consistent with movement on the NSTRs, but they appear to have to be located close to NSTRs (e.g., [134,135]). This observation suggests the possibility that the extension of the NSTRs was the response to a profound period of lithospheric evolution. Geophysical and geological investigations have unveiled the existence of slab tear within the Indian plate as it subducts underneath southern Tibet (e.g., [136,137]). Hou et al. [138] deem that the slab tear of the Indian plate due to the collision resulted in the upward movement of a significant volume of asthenosphere material. This phenomenon triggers the partial melting of lower crustal material (adakitic rock) and the upwelling asthenosphere mantle (ultrapotassic rock) which subsequently rise along the rift zones situated above the tear plate.

The slab tear model proposed by Bian et al. [50] can explain our above conclusion. In this scenario, lateral slab detachment pushed the eastward development of rifting, and the resultant slab tear induced the second stage of the activity. This model is essentially in agreement with the fault activity and the distribution characteristics of adakite and ultrapotassic rocks.

7. Conclusions

The STDS and NSTRs in the Yadong region of eastern Himalaya exhibit a cross-cutting relationship. New thermochronological data combined with thermokinematic numerical modeling of the footwall of these extensional structures reveal several significant findings:

1. The region has undergone five distinct phases of cooling since the middle Miocene, which included three pulses of faster exhumation caused by the slip on extensional structures.
2. There is notable diachronicity in the cessation of movement along the strike of the STDS, with the activity of the STDS leading to the first period of rapid exhumation-related cooling, which ceased at 12–11 Ma.
3. The Yadong fault initiated at approximately 12 Ma and experienced pulses of rapid exhumation between 6.2 and 4.7 Ma. These two periods of activity contributed to the rapid exhumation of the region in the middle Miocene and early Pliocene.

Supplementary Materials: The following supporting information can be downloaded at: <https://www.mdpi.com/article/10.3390/min14010066/s1>. References [113,139,140] are cited in the supplementary materials. The Supplementary Materials contain files of one DOCX, two tables. Text S1: detailed description of Pecube. Figure S1: Exhumation periods and transition times of each model. Figure S2: Scatterplots of the Pecube inversion results for models YD01, YD02, YD03, and YD05. Table S1: Summary of the age constraints of STDS and NSTRs across the Himalayan-Tibetan orogen. Some cells in the table, such as sample No or GPS, are not filled in because corresponding information is not available in the relevant literature; Table S2: Low-temperature thermochronological data for Pecube of our model.

Author Contributions: Conceptualization, Y.L. and T.X.; methodology, Z.M.; software, Y.J.; validation, W.B., B.Y. and T.X.; writing—original draft preparation, T.X.; writing—review and editing, F.M.S. and T.X. All authors have read and agreed to the published version of the manuscript.

Funding: This work was supported by the National Natural Science Foundation of China (Grant No. 91955206), the Second Tibetan Plateau Scientific Expedition and Research Program (STEP) (Grant No. 2019QZKK0803), the China Geological Survey (Grant No. DD20190057), the Fundamental Research Funds for the Central Universities (Grant No. 35732020071), and the National Natural Science Foundation of China (Grant No. 42302241).

Data Availability Statement: The data used to support the findings of this study are included within the Supplementary Materials.

Conflicts of Interest: The authors declare no conflicts of interest.

References

1. Mahéo, G.; Leloup, P.H.; Valli, F.; Lacassin, R.; Arnaud, N.; Paquette, J.L.; Fernandez, A.; Haibing, L.; Farley, K.A.; Tapponnier, P. Post 4 Ma initiation of normal faulting in southern Tibet. Constraints from the Kung Co half graben. *Earth Planet. Sci. Lett.* **2007**, *256*, 233–243. [[CrossRef](#)]
2. Hodges, K.V. Tectonics of the Himalaya and southern Tibet from two perspectives. *GSA Bull.* **2000**, *112*, 324–350. [[CrossRef](#)]
3. Wang, C.; Dai, J.; Zhao, X.; Li, Y.; Graham, S.A.; He, D.; Ran, B.; Meng, J. Outward-growth of the Tibetan Plateau during the Cenozoic: A review. *Tectonophysics* **2014**, *621*, 1–43. [[CrossRef](#)]
4. Burchfiel, B.C.; Zhiliang, C.; Hodges, K.V.; Yuping, L.; Royden, L.H.; Changrong, D.; Jiene, X.; Burchfiel, B.C.; Zhiliang, C.; Hodges, K.V.; et al. *The South Tibetan Detachment System, Himalayan Orogen: Extension Contemporaneous with and Parallel to Shortening in a Collisional Mountain Belt*; Geological Society of America: Boulder, CO, USA, 1992; Volume 269.
5. Hodges, K.V.; Parrish, R.R.; Housh, T.B.; Lux, D.R.; Burchfiel, B.C.; Royden, L.H.; Chen, Z. Simultaneous Miocene Extension and Shortening in the Himalayan Orogen. *Science* **1992**, *258*, 1466–1470. [[CrossRef](#)] [[PubMed](#)]
6. Yin, A. Cenozoic tectonic evolution of the Himalayan orogen as constrained by along-strike variation of structural geometry, exhumation history, and foreland sedimentation. *Earth-Sci. Rev.* **2006**, *76*, 1–131. [[CrossRef](#)]
7. Molnar, P.; Tapponnier, P. Active tectonics of Tibet. *J. Geophys. Res. Solid Earth* **1978**, *83*, 5361–5375. [[CrossRef](#)]
8. Pan, Y.; Kidd, W.S.F. Nyainqentanglha shear zone: A late Miocene extensional detachment in the southern Tibetan Plateau. *Geology* **1992**, *20*, 775–778. [[CrossRef](#)]
9. Molnar, P.; England, P.; Martinod, J. Mantle dynamics, uplift of the Tibetan Plateau, and the Indian Monsoon. *Rev. Geophys.* **1993**, *31*, 357–396. [[CrossRef](#)]
10. Styron, R.; Taylor, M.; Sundell, K. Accelerated extension of Tibet linked to the northward underthrusting of Indian crust. *Nat. Geosci.* **2015**, *8*, 131–134. [[CrossRef](#)]
11. Burg, J.P.; Brunel, M.; Gapais, D.; Chen, G.M.; Liu, G.H. Deformation of leucogranites of the crystalline Main Central Sheet in southern Tibet (China). *J. Struct. Geol.* **1984**, *6*, 535–542. [[CrossRef](#)]
12. Cooper, F.J.; Hodges, K.V.; Parrish, R.R.; Roberts, N.M.W.; Horstwood, M.S.A. Synchronous N-S and E-W extension at the Tibet-to-Himalaya transition in NW Bhutan. *Tectonics* **2015**, *34*, 1375–1395. [[CrossRef](#)]
13. Hintersberger, E.; Thiede, R.C.; Strecker, M.R.; Hacker, B.R. East-west extension in the NW Indian Himalaya. *GSA Bull.* **2010**, *122*, 1499–1515. [[CrossRef](#)]
14. Thiede, R.C.; Arrowsmith, J.R.N.; Bookhagen, B.; McWilliams, M.; Sobel, E.R.; Strecker, M.R. Dome formation and extension in the Tethyan Himalaya, Leo Pargil, northwest India. *GSA Bull.* **2006**, *118*, 635–650. [[CrossRef](#)]
15. Langille, J.M.; Jessup, M.J.; Cottle, J.M.; Lederer, G.; Ahmad, T. Timing of metamorphism, melting and exhumation of the Leo Pargil dome, northwest India. *J. Metamorph. Geol.* **2012**, *30*, 769–791. [[CrossRef](#)]
16. McCallister, A.T.; Taylor, M.H.; Murphy, M.A.; Styron, R.H.; Stockli, D.F. Thermochronologic constraints on the late Cenozoic exhumation history of the Gurla Mandhata metamorphic core complex, Southwestern Tibet. *Tectonics* **2014**, *33*, 27–52. [[CrossRef](#)]
17. Murphy, M.A.; Yin, A.; Kapp, P.; Harrison, T.M.; Manning, C.E.; Ryerson, F.J.; Lin, D.; Jinghui, G. Structural evolution of the Gurla Mandhata detachment system, southwest Tibet: Implications for the eastward extent of the Karakoram fault system. *GSA Bull.* **2002**, *114*, 428–447. [[CrossRef](#)]
18. Murphy, M.A.; Copeland, P. Transensional deformation in the central Himalaya and its role in accommodating growth of the Himalayan orogen. *Tectonics* **2005**, *24*, TC4012. [[CrossRef](#)]
19. Li, H. *The Initial Timing, Extension Rates of the N-S Trends Normal Faults in Tibetan Plateau and its Deep Process and Dynamics*; China University of Geosciences: Beijing, China, 2020.
20. Woodruff, W.H., Jr.; Horton, B.K.; Kapp, P.; Stockli, D.F. Late Cenozoic evolution of the Lunggar extensional basin, Tibet: Implications for basin growth and exhumation in hinterland plateaus. *GSA Bull.* **2013**, *125*, 343–358. [[CrossRef](#)]
21. Sundell, K.E.; Taylor, M.H.; Styron, R.H.; Stockli, D.F.; Kapp, P.; Hager, C.; Liu, D.; Ding, L. Evidence for constriction and Pliocene acceleration of east-west extension in the North Lunggar rift region of west central Tibet. *Tectonics* **2013**, *32*, 1454–1479. [[CrossRef](#)]
22. Styron, R.H.; Taylor, M.H.; Sundell, K.E.; Stockli, D.F.; Oalman, J.A.G.; Möller, A.; McCallister, A.T.; Liu, D.; Ding, L. Miocene initiation and acceleration of extension in the South Lunggar rift, western Tibet: Evolution of an active detachment system from structural mapping and (U-Th)/He thermochronology. *Tectonics* **2013**, *32*, 880–907. [[CrossRef](#)]
23. Larson, K.P.; Kellett, D.A.; Cottle, J.M.; Camacho, A.; Brubacher, A.D. Mid-Miocene initiation of E-W extension and recoupling of the Himalaya. *Terra Nova* **2020**, *32*, 151–158. [[CrossRef](#)]
24. Garzzone, C.N.; DeCelles, P.G.; Hodkinson, D.G.; Ojha, T.P.; Upreti, B.N. East-west extension and Miocene environmental change in the southern Tibetan plateau: Thakkhola graben, central Nepal. *GSA Bull.* **2003**, *115*, 3–20. [[CrossRef](#)]
25. Garzzone, C.N.; Dettman, D.L.; Quade, J.; DeCelles, P.G.; Butler, R.F. High times on the Tibetan Plateau: Paleoelevation of the Thakkhola graben, Nepal. *Geology* **2000**, *28*, 339–342. [[CrossRef](#)]
26. Coleman, M.; Hodges, K. Evidence for Tibetan plateau uplift before 14 Myr ago from a new minimum age for east–west extension. *Nature* **1995**, *374*, 49–52. [[CrossRef](#)]
27. Laskowski, A.K.; Kapp, P.; Ding, L.; Campbell, C.; Liu, X. Tectonic evolution of the Yarlung suture zone, Lopu Range region, southern Tibet. *Tectonics* **2017**, *36*, 108–136. [[CrossRef](#)]
28. Sanchez, V.I.; Murphy, M.A.; Robinson, A.C.; Lapen, T.J.; Heizler, M.T. Tectonic evolution of the India–Asia suture zone since Middle Eocene time, Lopukangri area, south-central Tibet. *J. Asian Earth Sci.* **2013**, *62*, 205–220. [[CrossRef](#)]

29. Shen, T.; Wang, G.; Leloup, P.H.; van der Beek, P.; Bernet, M.; Cao, K.; Wang, A.; Liu, C.; Zhang, K. Controls on Cenozoic exhumation of the Tethyan Himalaya from fission-track thermochronology and detrital zircon U-Pb geochronology in the Gyirong basin area, southern Tibet. *Tectonics* **2016**, *35*, 1713–1734. [[CrossRef](#)]
30. Mitsuishi, M.; Wallis, S.R.; Aoya, M.; Lee, J.; Wang, Y. E–W extension at 19 Ma in the Kung Co area, S. Tibet: Evidence for contemporaneous E–W and N–S extension in the Himalayan orogen. *Earth Planet. Sci. Lett.* **2012**, *325–326*, 10–20. [[CrossRef](#)]
31. Lee, J.; Hager, C.; Wallis, S.R.; Stockli, D.F.; Whitehouse, M.J.; Aoya, M.; Wang, Y. Middle to late Miocene extremely rapid exhumation and thermal reequilibration in the Kung Co rift, southern Tibet. *Tectonics* **2011**, *30*, TC2007. [[CrossRef](#)]
32. Dewane, T.J.; Stockli, D.F.; Hager, C.; Taylor, M.; Ding, L.; Lee, J.; Wallis, S. Timing of Cenozoic E–W Extension in the Tangra Yum Co–Kung Co Rift, south-central Tibet. *Eos. Trans. AGU Fall Meet. Suppl.* **2006**, *87*, T34C-04.
33. Wolff, R.; Hetzel, R.; Dunkl, I.; Xu, Q.; Bröcker, M.; Anczkiewicz, A.A. High-Angle Normal Faulting at the Tangra Yumco Graben (Southern Tibet) since ~15 Ma. *J. Geol.* **2019**, *127*, 15–36. [[CrossRef](#)]
34. Blisniuk, P.M.; Hacker, B.R.; Glodny, J.; Ratschbacher, L.; Bi, S.; Wu, Z.; McWilliams, M.O.; Calvert, A. Normal faulting in central Tibet since at least 13.5 Myr ago. *Nature* **2001**, *412*, 628–632. [[CrossRef](#)] [[PubMed](#)]
35. Cottle, J.M.; Jessup, M.J.; Newell, D.L.; Horstwood, M.S.A.; Noble, S.R.; Parrish, R.R.; Waters, D.J.; Searle, M.P. Geochronology of granulitized eclogite from the Ama Drime Massif: Implications for the tectonic evolution of the South Tibetan Himalaya. *Tectonics* **2009**, *28*, TC1002. [[CrossRef](#)]
36. Kali, E.; Leloup, P.H.; Arnaud, N.; Mahéo, G.; Liu, D.; Boutonnet, E.; Van der Woerd, J.; Liu, X.; Liu-Zeng, J.; Li, H. Exhumation history of the deepest central Himalayan rocks, Ama Drime range: Key pressure-temperature-deformation-time constraints on orogenic models. *Tectonics* **2010**, *29*, TC2014. [[CrossRef](#)]
37. Zhang, J.; Guo, L. Structure and geochronology of the southern Xainza–Dinggye rift and its relationship to the south Tibetan detachment system. *J. Asian Earth Sci.* **2007**, *29*, 722–736. [[CrossRef](#)]
38. Hager, C.; Stockli, D.; Dewane, T.; Gehrels, G.; Ding, L. Anatomy and crustal evolution of the central Lhasa terrane (S-Tibet) revealed by investigations in the Xainza rift. In Proceedings of the EGU General Assembly Conference Abstracts, Vienna, Austria, 1 April 2009; p. 11346.
39. Orme, D.A. Burial and exhumation history of the Xigaze forearc basin, Yarlung suture zone, Tibet. *Geosci. Front.* **2019**, *10*, 895–908. [[CrossRef](#)]
40. Jessup, M.J.; Newell, D.L.; Cottle, J.M.; Berger, A.L.; Spotila, J.A. Orogen-parallel extension and exhumation enhanced by denudation in the trans-Himalayan Arun River gorge, Ama Drime Massif, Tibet–Nepal. *Geology* **2008**, *36*, 587–590. [[CrossRef](#)]
41. Hager, C. *Integrated Tectonic and Quantitative Thermochronometric Investigation of the Xainza Rift, Tibet*; University of Kansas: Lawrence, KS, USA, 2014.
42. Ratschbacher, L.; Krumrei, I.; Blumenwitz, M.; Staiger, M.; Gloaguen, R.; Miller, B.V.; Samson, S.D.; Edwards, M.A.; Appel, E. Rifting and strike-slip shear in central Tibet and the geometry, age and kinematics of upper crustal extension in Tibet. *Geol. Soc. Lond. Spec. Publ.* **2011**, *353*, 127–163. [[CrossRef](#)]
43. Wu, Z.; Jiang, W.; Zhou, J.; Li, Y. Thermochronological analysis of the thermal history and tectonic geomorphological evolution process of typical rock masses in the hinterland of the Qinghai Tibet Plateau. *Acta Geol. Sin.* **2001**, *75*, 468–476.
44. Wu, Z.; Jiang, W.; Wu, Z.; Zhang, S. Dating of Typical Basin and Range Tectonics in Central Tibetan Plateau. *Acta Geosci. Sin.* **2002**, *23*, 6.
45. Harrison, T.M.; Copeland, P.; Kidd, W.S.F.; Lovera, O.M. Activation of the Nyainqentanghla Shear Zone: Implications for uplift of the southern Tibetan Plateau. *Tectonics* **1995**, *14*, 658–676. [[CrossRef](#)]
46. Edwards, M.A.; Harrison, T.M. When did the roof collapse? Late Miocene north-south extension in the high Himalaya revealed by Th–Pb monazite dating of the Khula Kangri granite. *Geology* **1997**, *25*, 543–546. [[CrossRef](#)]
47. Wang, S. *Study on the Tectonic Geomorphology and Active Timing of Yadong Rift, Southern Tibet*; China University of Geosciences: Beijing, China, 2020.
48. HA, G.; WU, Z.; HE, L.; WANG, S. Late Cenozoic sedimentary evolution of Pagri–Duoqing Co graben, southern end of Yadong–Gulu Rift, Southern Tibet. *Acta Geol. Sin.-Engl. Ed.* **2018**, *92*, 972–987. [[CrossRef](#)]
49. Antolín, B.; Schill, E.; Grujic, D.; Baule, S.; Quidelleur, X.; Appel, E.; Waldhör, M. E–W extension and block rotation of the southeastern Tibet: Unravelling late deformation stages in the eastern Himalayas (NW Bhutan) by means of pyrrhotite remanences. *J. Struct. Geol.* **2012**, *42*, 19–33. [[CrossRef](#)]
50. Bian, S.; Gong, J.; Zuza, A.V.; Yang, R.; Chen, L.; Ji, J.; Yu, X.; Tian, Y.; Yu, Z.; Cheng, X.; et al. Along-Strike Variation in the Initiation Timing of the North-Trending Rifts in Southern Tibet as Revealed from the Yadong–Gulu Rift. *Tectonics* **2022**, *41*, e2021TC007091. [[CrossRef](#)]
51. Stockli, D.; Taylor, M.; Yin, A.; Harrison, M.; D’Andrea, J.; Kapp, P.; Ding, L. Late Miocene–Pliocene inception of E–W extension in Tibet as evidenced by apatite (U–Th)/He data. *Geol. Soc. Am. Abstr.* **2002**, *34*, 182–188.
52. Shen, T.; Wang, G.; van der Beek, P.; Bernet, M.; Chen, Y.; Zhang, P.; Wang, A.; Cao, K. Impacts of late Miocene normal faulting on Yarlung Tsangpo River evolution, southeastern Tibet. *GSA Bull.* **2022**, *134*, 3142–3154. [[CrossRef](#)]
53. Bian, S.; Gong, J.; Zuza, A.V.; Yang, R.; Tian, Y.; Ji, J.; Chen, H.; Xu, Q.; Chen, L.; Lin, X.; et al. Late Pliocene onset of the Cona rift, eastern Himalaya, confirms eastward propagation of extension in Himalayan–Tibetan orogen. *Earth Planet. Sci. Lett.* **2020**, *544*, 116383. [[CrossRef](#)]

54. Walker, J.D.; Martin, M.W.; Bowring, S.A.; Searle, M.P.; Waters, D.J.; Hodges, K.V. Metamorphism, Melting, and Extension: Age Constraints from the High Himalayan Slab of Southeast Zaskar and Northwest Lahaul. *J. Geol.* **1999**, *107*, 473–495. [[CrossRef](#)]
55. Vannay, J.-C.; Grasemann, B.; Rahn, M.; Frank, W.; Carter, A.; Baudraz, V.; Cosca, M. Miocene to Holocene exhumation of metamorphic crustal wedges in the NW Himalaya: Evidence for tectonic extrusion coupled to fluvial erosion. *Tectonics* **2004**, *23*, TC1014. [[CrossRef](#)]
56. Searle, M.P.; Noble, S.R.; Hurford, A.J.; Rex, D.C. Age of crustal melting, emplacement and exhumation history of the Shivling leucogranite, Garhwal Himalaya. *Geol. Mag.* **1999**, *136*, 513–525. [[CrossRef](#)]
57. Guillot, S.P.; Hodges, K.; Fort, P.L.; Pecher, A. New constraints on the age of the Manaslu leucogranite: Evidence for episodic tectonic denudation in the central Himalayas. *Geology* **1994**, *22*, 559–562. [[CrossRef](#)]
58. Searle, M.P.; Parrish, R.R.; Hodges, K.V.; Hurford, A.; Ayres, M.W.; Whitehouse, M.J. Shisha Pangma Leucogranite, South Tibetan Himalaya: Field Relations, Geochemistry, Age, Origin, and Emplacement. *J. Geol.* **1997**, *105*, 295–318. [[CrossRef](#)]
59. Sakai, H.; Sawada, M.; Takigami, Y.; Orihashi, Y.; Danhara, T.; Iwano, H.; Kuwahara, Y.; Dong, Q.; Cai, H.; Li, J. Geology of the summit limestone of Mount Qomolangma (Everest) and cooling history of the Yellow Band under the Qomolangma detachment. *Isl. Arc* **2005**, *14*, 297–310. [[CrossRef](#)]
60. Cottle, J.M.; Waters, D.J.; Riley, D.; Beyssac, O.; Jessup, M.J. Metamorphic history of the South Tibetan Detachment System, Mt. Everest region, revealed by RSCM thermometry and phase equilibria modelling. *J. Metamorph. Geol.* **2011**, *29*, 561–582. [[CrossRef](#)]
61. Leloup, P.H.; Mahéo, G.; Arnaud, N.; Kali, E.; Boutonnet, E.; Liu, D.; Xiaohan, L.; Haibing, L. The South Tibet detachment shear zone in the Dinggye area: Time constraints on extrusion models of the Himalayas. *Earth Planet. Sci. Lett.* **2010**, *292*, 1–16. [[CrossRef](#)]
62. Jessup, M.J.; Cottle, J.M. Progression from South-Directed Extrusion to Orogen-Parallel Extension in the Southern Margin of the Tibetan Plateau, Mount Everest Region, Tibet. *J. Geol.* **2010**, *118*, 467–486. [[CrossRef](#)]
63. Gu, D.; Zhang, J.; Lin, C.; Fan, Y.; Feng, L.; Zheng, J. Geochronological and metamorphic constraints on the exhumation of the Ama Drime Massif: Implications for the mid-Miocene evolution of Himalayan extensional structures. *Tectonophysics* **2022**, *836*, 229408. [[CrossRef](#)]
64. Kellett, D.A.; Grujic, D.; Coutand, I.; Cottle, J.; Mukul, M. The South Tibetan detachment system facilitates ultra rapid cooling of granulite-facies rocks in Sikkim Himalaya. *Tectonics* **2013**, *32*, 252–270. [[CrossRef](#)]
65. Montomoli, C.; Carosi, R.; Rubatto, D.; Visonà, D.; Iaccarino, S. Tectonic activity along the inner margin of the South Tibetan Detachment constrained by syntectonic leucogranite emplacement in Western Bhutan. *Ital. J. Geosci.* **2017**, *136*, 5–14. [[CrossRef](#)]
66. Kellett, D.A.; Grujic, D.; Erdmann, S. Miocene structural reorganization of the South Tibetan detachment, eastern Himalaya: Implications for continental collision. *Lithosphere* **2009**, *1*, 259–281. [[CrossRef](#)]
67. Kellett, D.A.; Grujic, D.; Warren, C.; Cottle, J.; Jamieson, R.; Tenzin, T. Metamorphic history of a syn-convergent orogen-parallel detachment: The South Tibetan detachment system, Bhutan Himalaya. *J. Metamorph. Geol.* **2010**, *28*, 785–808. [[CrossRef](#)]
68. Chambers, J.; Parrish, R.; Argles, T.; Harris, N.; Horstwood, M. A short-duration pulse of ductile normal shear on the outer South Tibetan detachment in Bhutan: Alternating channel flow and critical taper mechanics of the eastern Himalaya. *Tectonics* **2011**, *30*, TC2005. [[CrossRef](#)]
69. Maluski, H.; Matte, P.; Brunel, M.; Xiao, X. Argon 39-argon 40 dating of metamorphic and plutonic events in the north and high Himalaya belts (southern Tibet-China). *Tectonics* **1988**, *7*, 299–326. [[CrossRef](#)]
70. Grujic, D.; Coutand, I.; Bookhagen, B.; Bonnet, S.P.; Blythe, A.; Duncan, C. Climatic forcing of erosion, landscape, and tectonics in the Bhutan Himalayas. *Geology* **2006**, *34*, 801–804. [[CrossRef](#)]
71. Grujic, D.; Warren, C.J.; Wooden, J.L. Rapid synconvergent exhumation of Miocene-aged lower orogenic crust in the eastern Himalaya. *Lithosphere* **2011**, *3*, 346–366. [[CrossRef](#)]
72. Warren, C.J.; Grujic, D.; Kellett, D.A.; Cottle, J.; Jamieson, R.A.; Ghalley, K.S. Probing the depths of the India-Asia collision: U-Th-Pb monazite chronology of granulites from NW Bhutan. *Tectonics* **2011**, *30*, TC2004. [[CrossRef](#)]
73. Carosi, R.; Lombardo, B.; Molli, G.; Musumeci, G.; Pertusati, P.C. The south Tibetan detachment system in the Rongbuk valley, Everest region. Deformation features and geological implications. *J. Asian Earth Sci.* **1998**, *16*, 299–311. [[CrossRef](#)]
74. Cooper, F.J.; Adams, B.A.; Edwards, C.S.; Hodges, K.V. Large normal-sense displacement on the South Tibetan fault system in the eastern Himalaya. *Geology* **2012**, *40*, 971–974. [[CrossRef](#)]
75. Liu, Z.-C.; Wu, F.-Y.; Qiu, Z.-L.; Wang, J.-G.; Liu, X.-C.; Ji, W.-Q.; Liu, C.-Z. Leucogranite geochronological constraints on the termination of the South Tibetan Detachment in eastern Himalaya. *Tectonophysics* **2017**, *721*, 106–122. [[CrossRef](#)]
76. Stübner, K.; Grujic, D.; Parrish, R.R.; Roberts, N.M.W.; Kronz, A.; Wooden, J.; Ahmad, T. Monazite geochronology unravels the timing of crustal thickening in NW Himalaya. *Lithos* **2014**, *210–211*, 111–128. [[CrossRef](#)]
77. Carosi, R.; Montomoli, C.; Rubatto, D.; Visonà, D. Leucogranite intruding the South Tibetan Detachment in western Nepal: Implications for exhumation models in the Himalayas. *Terra Nova* **2013**, *25*, 478–489. [[CrossRef](#)]
78. Molnar, P.; Tapponnier, P. Cenozoic Tectonics of Asia: Effects of a Continental Collision. *Science* **1975**, *189*, 419–426. [[CrossRef](#)] [[PubMed](#)]
79. Taylor, M.; Yin, A. Active structures of the Himalayan-Tibetan orogen and their relationships to earthquake distribution, contemporary strain field, and Cenozoic volcanism. *Geosphere* **2009**, *5*, 199–214. [[CrossRef](#)]

80. Nania, L.; Montomoli, C.; Iaccarino, S.; Vincenzo, G.D.; Carosi, R. A thermal event in the Dolpo region (Nepal): A consequence of the shift from orogen perpendicular to orogen parallel extension in central Himalaya? *J. Geol. Soc.* **2022**, *179*, jgs2020–jgs2261. [[CrossRef](#)]
81. Gong, J.; Ji, J.; Han, B.; Chen, J.; Sun, D.; Li, B.; Zhou, J.; Tu, J.; Zhong, D. Early subduction–exhumation and late channel flow of the Greater Himalayan Sequence: Implications from the Yadong section in the eastern Himalaya. *Int. Geol. Rev.* **2012**, *54*, 1184–1202. [[CrossRef](#)]
82. Wang, A.; Min, K.; Wang, G.; Cao, K.; Shen, T.; Jiang, P.; Wei, J. Slow exhumation of the Greater Himalaya in the Yadong region, the transition between the Central and Eastern Himalaya, during the Late Neogene. *J. Geol. Soc.* **2019**, *176*, 1207–1217. [[CrossRef](#)]
83. Dong, H.; Larson, K.P.; Kellett, D.A.; Xu, Z.; Li, G.; Cao, H.; Yi, Z.; Zeng, L. Timing of slip across the South Tibetan detachment system and Yadong–Gulu graben, Eastern Himalaya. *J. Geol. Soc.* **2020**, *178*, jgs2019–jgs2197. [[CrossRef](#)]
84. Wagner, G.A.; van den Haute, P. *Fission-Track Dating*; Kluwer: Alphen aan den Rijn, The Netherlands, 1992.
85. Bernet, M. A field-based estimate of the zircon fission-track closure temperature. *Chem. Geol.* **2009**, *259*, 181–189. [[CrossRef](#)]
86. Wagner, G.A.; Reimer, G.M.; Jäger, E. *Cooling Ages Derived by Apatite Fission-Track, Mica Rb-Sr and K-Ar Dating: The Uplift and Cooling History of the Central Alps*; Società Cooperativa Tipografica: Padova, Italy, 1977.
87. Wagner, G.A.; Reimer, G.M. Fission track tectonics: The tectonic interpretation of fission track apatite ages. *Earth Planet. Sci. Lett.* **1972**, *14*, 263–268. [[CrossRef](#)]
88. Yin, A.; Harrison, T.M. Geologic Evolution of the Himalayan-Tibetan Orogen. *Annu. Rev. Earth Planet. Sci.* **2000**, *28*, 211–280. [[CrossRef](#)]
89. Kellett, D.A.; Cottle, J.M.; Larson, K.P. The South Tibetan Detachment System: History, advances, definition and future directions. *Geol. Soc. Lond. Spec. Publ.* **2019**, *483*, 377–400. [[CrossRef](#)]
90. Le Fort, P. Himalayas: The collided range. Present knowledge of the continental arc. *Am. J. Sci.* **1975**, *275*, 144.
91. Searle, M.P.; Law, R.D.; Godin, L.; Larson, K.P.; Streule, M.J.; Cottle, J.M.; Jessup, M.J. Defining the Himalayan Main Central Thrust in Nepal. *J. Geol. Soc.* **2008**, *165*, 523–534. [[CrossRef](#)]
92. Allègre, C.J.; Courtillot, V.; Tapponnier, P.; Hirn, A.; Mattauer, M.; Coulon, C.; Jaeger, J.J.; Achache, J.; Schärer, U.; Marcoux, J.; et al. Structure and evolution of the Himalaya–Tibet orogenic belt. *Nature* **1984**, *307*, 17–22. [[CrossRef](#)]
93. Long, S.; McQuarrie, N.; Tobgay, T.; Grujic, D.; Hollister, L. Geologic Map of Bhutan. *J. Maps* **2011**, *7*, 184–192. [[CrossRef](#)]
94. Kellett, D.A.; Grujic, D. New insight into the South Tibetan detachment system: Not a single progressive deformation. *Tectonics* **2012**, *31*, TC2007. [[CrossRef](#)]
95. Searle, M.P.; Simpson, R.L.; Law, R.D.; Parrish, R.R.; Waters, D.J. The structural geometry, metamorphic and magmatic evolution of the Everest massif, High Himalaya of Nepal–South Tibet. *J. Geol. Soc.* **2003**, *160*, 345–366. [[CrossRef](#)]
96. Jessup, M.J.; Cottle, J.M.; Searle, M.P.; Law, R.D.; Newell, D.L.; Tracy, R.J.; Waters, D.J. P–T–t–D paths of Everest Series schist, Nepal. *J. Metamorph. Geol.* **2008**, *26*, 717–739. [[CrossRef](#)]
97. Law, R.D.; Jessup, M.J.; Searle, M.P.; Francis, M.K.; Waters, D.J.; Cottle, J.M. Telescoping of isotherms beneath the South Tibetan Detachment System, Mount Everest Massif. *J. Struct. Geol.* **2011**, *33*, 1569–1594. [[CrossRef](#)]
98. Leger, R.M.; Webb, A.A.G.; Henry, D.J.; Craig, J.A.; Dubey, P. Metamorphic field gradients across the Himachal Himalaya, northwest India: Implications for the emplacement of the Himalayan crystalline core. *Tectonics* **2013**, *32*, 540–557. [[CrossRef](#)]
99. Carosi, R.; Montomoli, C.; Visonà, D. Is there any detachment in the Lower Dolpo (western Nepal)? *Comptes Rendus Geosci.* **2002**, *334*, 933–940. [[CrossRef](#)]
100. Montomoli, C.; Iaccarino, S.; Antolin, B.; Appel, E.; Carosi, R.; Dunkl, I.; Lin, D.; Visonà, D. Tectono-metamorphic evolution of the Tethyan Sedimentary Sequence (Himalayas, SE Tibet). *Ital. J. Geosci.* **2017**, *136*, 73–88. [[CrossRef](#)]
101. Dunkl, I.; Antolín, B.; Wemmer, K.; Rantitsch, G.; Kienast, M.; Montomoli, C.; Ding, L.; Carosi, R.; Appel, E.; Bay, R.E.; et al. Metamorphic evolution of the Tethyan Himalayan flysch in SE Tibet. *Geol. Soc. Lond. Spec. Publ.* **2011**, *353*, 45–69. [[CrossRef](#)]
102. Sylvester, P.J. Post-collisional strongly peraluminous granites. *Lithos* **1998**, *45*, 29–44. [[CrossRef](#)]
103. Visonà, D.; Lombardo, B. Two-mica and tourmaline leucogranites from the Everest–Makalu region (Nepal–Tibet). Himalayan leucogranite genesis by isobaric heating? *Lithos* **2002**, *62*, 125–150. [[CrossRef](#)]
104. Searle, M.P.; Cottle, J.M.; Streule, M.J.; Waters, D.J. Crustal melt granites and migmatites along the Himalaya: Melt source, segregation, transport and granite emplacement mechanisms. *Earth Environ. Sci. Trans. R. Soc. Edinb.* **2009**, *100*, 219–233. [[CrossRef](#)]
105. Tapponnier, P.; Mercier, J.L.; Armijo, R.; Tonglin, H.; Ji, Z. Field evidence for active normal faulting in Tibet. *Nature* **1981**, *294*, 410–414. [[CrossRef](#)]
106. Guo, X.; Gao, R.; Zhao, J.; Xu, X.; Lu, Z.; Klemperer, S.L.; Liu, H. Deep-seated lithospheric geometry in revealing collapse of the Tibetan Plateau. *Earth-Sci. Rev.* **2018**, *185*, 751–762. [[CrossRef](#)]
107. Yan, H.; Long, X.; Li, J.; Wang, Q.; Wang, X.-C.; Wu, B.; Wang, J.; Gou, L. Miocene adakites in south Tibet: Partial melting of the thickened Lhasa juvenile mafic lower crust with the involvement of ancient Indian continental crust compositions. *GSA Bull.* **2019**, *132*, 1273–1290. [[CrossRef](#)]
108. Wang, R.; Richards, J.P.; Zhou, L.-M.; Hou, Z.-Q.; Stern, R.A.; Creaser, R.A.; Zhu, J.-J. The role of Indian and Tibetan lithosphere in spatial distribution of Cenozoic magmatism and porphyry Cu–Mo deposits in the Gangdese belt, southern Tibet. *Earth-Sci. Rev.* **2015**, *150*, 68–94. [[CrossRef](#)]

109. Ji, J.Q.; Zhong, D.L.; Song, B.; Chu, M.F.; Wen, D.J. Metamorphism, geochemistry and U-Pb zircon SHRIMP geochronology of the high-pressure granulites in the central Greater Himalayas. *Acta Petrol. Sin.* **2004**, *20*, 1283–1300.
110. Bellemans, F.; De Corte, F.; Van, D.; Haute, P. Composition of srm and cn u-doped glasses: Significance for their use as thermal neutron fluence monitors in fission track dating. *Radiat. Meas.* **1995**, *24*, 153–160. [[CrossRef](#)]
111. Hurford, A.J.; Green, P.F. The zeta age calibration of fission-track dating. *Chem. Geol.* **1983**, *41*, 285–317. [[CrossRef](#)]
112. Hurford, A.J. Standardization of fission track dating calibration: Recommendation by the Fission Track Working Group of the I.U.G.S. Subcommittee on Geochronology. *Chem. Geol. Isot. Geosci. Sect.* **1990**, *80*, 171–178. [[CrossRef](#)]
113. Braun, J. Pecube: A new finite-element code to solve the 3D heat transport equation including the effects of a time-varying, finite amplitude surface topography. *Comput. Geosci.* **2003**, *29*, 787–794. [[CrossRef](#)]
114. Vermeesch, P. RadialPlotter: A Java application for fission track, luminescence and other radial plots. *Radiat. Meas. Radiat Meas* **2009**, *44*, 409–410. [[CrossRef](#)]
115. Gleadow, A.J.W.; Duddy, I.R.; Green, P.F.; Lovering, J.F. Confined fission track lengths in apatite: A diagnostic tool for thermal history analysis. *Contrib. Mineral. Petrol.* **1986**, *94*, 405–415. [[CrossRef](#)]
116. Su, W.; He, Z.; Zhong, L.; Glorie, S.; Zhong, K.; Jepson, G.; De Grave, J. Late Oligocene—Miocene morpho-tectonic evolution of the central Gangdese batholith constrained by low-temperature thermochronology. *Tectonophysics* **2022**, *840*, 229559. [[CrossRef](#)]
117. Thiede, R.C. Tectonic and Climatic Controls on Orogenic Processes: The Northwest Himalaya, India. Ph.D. Thesis, Universität Potsdam, Potsdam, Germany, 2005.
118. Zeng, L.; Gao, L.-E.; Xie, K.; Liu-Zeng, J. Mid-Eocene high Sr/Y granites in the Northern Himalayan Gneiss Domes: Melting thickened lower continental crust. *Earth Planet. Sci. Lett.* **2011**, *303*, 251–266. [[CrossRef](#)]
119. Hou, Z.-Q.; Zheng, Y.-C.; Zeng, L.-S.; Gao, L.-E.; Huang, K.-X.; Li, W.; Li, Q.-Y.; Fu, Q.; Liang, W.; Sun, Q.-Z. Eocene–Oligocene granitoids in southern Tibet: Constraints on crustal anatexis and tectonic evolution of the Himalayan orogen. *Earth Planet. Sci. Lett.* **2012**, *349–350*, 38–52. [[CrossRef](#)]
120. Ketcham, R.A.; Carter, A.; Donelick, R.A.; Barbarand, J.; Hurford, A.J. Improved modeling of fission-track annealing in apatite. *Am. Mineral.* **2007**, *92*, 799–810. [[CrossRef](#)]
121. Braun, J.; van der Beek, P.; Valla, P.; Robert, X.; Herman, F.; Glotzbach, C.; Pedersen, V.; Perry, C.; Simon-Labric, T.; Prigent, C. Quantifying rates of landscape evolution and tectonic processes by thermochronology and numerical modeling of crustal heat transport using PECUBE. *Tectonophysics* **2012**, *524–525*, 1–28. [[CrossRef](#)]
122. Chen, B.; Liu, J.; Kaban, M.K.; Sun, Y.; Chen, C.; Du, J. Elastic thickness, mechanical anisotropy and deformation of the southeastern Tibetan Plateau. *Tectonophysics* **2014**, *637*, 45–56. [[CrossRef](#)]
123. Valla, P.G.; Herman, F.; van der Beek, P.A.; Braun, J. Inversion of thermochronological age-elevation profiles to extract independent estimates of denudation and relief history—I: Theory and conceptual model. *Earth Planet. Sci. Lett.* **2010**, *295*, 511–522. [[CrossRef](#)]
124. Carrapa, B.; Robert, X.; DeCelles, P.G.; Orme, D.A.; Thomson, S.N.; Schoenbohm, L.M. Asymmetric exhumation of the Mount Everest region: Implications for the tectono-topographic evolution of the Himalaya. *Geology* **2016**, *44*, 611–614. [[CrossRef](#)]
125. Naito, N.; Ageta, Y.; Iwata, S.; Matsuda, Y.; Suzuki, R.; Karma; Yabuki, H. Glacier shrinkages and climate conditions around Jichu Dramo Glacier in the Bhutan Himalayas from 1998 to 2003. *Bull. Glaciol. Res.* **2006**, *23*, 51–61.
126. Hodges, K.; Bowring, S.; Davidek, K.; Hawkins, D.; Krol, M. Evidence for rapid displacement on Himalayan normal faults and the importance of tectonic denudation in the evolution of mountain ranges. *Geology* **1998**, *26*, 483–486. [[CrossRef](#)]
127. Murphy, M.A.; Mark Harrison, T. Relationship between leucogranites and the Qomolangma detachment in the Rongbuk Valley, south Tibet. *Geology* **1999**, *27*, 831–834. [[CrossRef](#)]
128. Simpson, R.L.; Parrish, R.R.; Searle, M.P.; Waters, D.J. Two episodes of monazite crystallization during metamorphism and crustal melting in the Everest region of the Nepalese Himalaya. *Geology* **2000**, *28*, 403–406. [[CrossRef](#)]
129. Schultz, M.H.; Hodges, K.V.; Ehlers, T.A.; van Soest, M.; Wartho, J.-A. Thermochronologic constraints on the slip history of the South Tibetan detachment system in the Everest region, southern Tibet. *Earth Planet. Sci. Lett.* **2017**, *459*, 105–117. [[CrossRef](#)]
130. Webb, A.A.G.; Guo, H.; Clift, P.D.; Husson, L.; Müller, T.; Costantino, D.; Yin, A.; Xu, Z.; Cao, H.; Wang, Q. The Himalaya in 3D: Slab dynamics controlled mountain building and monsoon intensification. *Lithosphere* **2017**, *9*, 637–651. [[CrossRef](#)]
131. He, L. Sedimentary Evolution and Its Tectonic significances of the Pali Basin in Yadong County, Southern Tibet. Master Thesis, China University of Geosciences, Beijing, China, 2018.
132. Wang, S.; Shen, X.; Chevalier, M.-L.; Replumaz, A.; Zheng, Y.; Li, H.; Pan, J.; Li, K.; Xu, X. Illite K-Ar and (U-Th)/He low-temperature thermochronology reveal onset timing of Yadong-Gulu rift in southern Tibetan Plateau. *Front. Earth Sci.* **2022**, *10*, 993796. [[CrossRef](#)]
133. Wolff, R.; Hetzel, R.; Hölzer, K.; Dunkl, I.; Xu, Q.; Anczkiewicz, A.A.; Li, Z. Rift propagation in south Tibet controlled by under-thrusting of India: A case study of the Tangra Yumco graben (south Tibet). *J. Geol. Soc.* **2023**, *180*, jgs2022–jgs2090. [[CrossRef](#)]
134. Li, Y.; Li, X.; Wang, C.; Wei, Y.; Chen, X.; He, J.; Xu, M.; Hou, Y. Miocene adakitic intrusions in the Zhongba terrane: Implications for the origin and geochemical variations of post-collisional adakitic rocks in southern Tibet. *Gondwana Res.* **2017**, *41*, 65–76. [[CrossRef](#)]
135. Tian, S.-H.; Yang, Z.-S.; Hou, Z.-Q.; Mo, X.-X.; Hu, W.-J.; Zhao, Y.; Zhao, X.-Y. Subduction of the Indian lower crust beneath southern Tibet revealed by the post-collisional potassic and ultrapotassic rocks in SW Tibet. *Gondwana Res.* **2017**, *41*, 29–50. [[CrossRef](#)]

136. Liang, X.; Chen, Y.; Tian, X.; Chen, Y.J.; Ni, J.; Gallegos, A.; Klemperer, S.L.; Wang, M.; Xu, T.; Sun, C.; et al. 3D imaging of subducting and fragmenting Indian continental lithosphere beneath southern and central Tibet using body-wave finite-frequency tomography. *Earth Planet. Sci. Lett.* **2016**, *443*, 162–175. [[CrossRef](#)]
137. Wang, G.; Wei, W.; Ye, G.; Jin, S.; Jing, J.; Zhang, L.; Dong, H.; Xie, C.; Omisore, B.O.; Guo, Z. 3-D electrical structure across the Yadong-Gulu rift revealed by magnetotelluric data: New insights on the extension of the upper crust and the geometry of the underthrusting Indian lithospheric slab in southern Tibet. *Earth Planet. Sci. Lett.* **2017**, *474*, 172–179. [[CrossRef](#)]
138. Hou, Z.; Yang, Z.; Lu, Y.; Kemp, A.; Zheng, Y.; Li, Q.; Tang, J.; Yang, Z.; Duan, L. A genetic linkage between subduction- and collision-related porphyry Cu deposits in continental collision zones. *Geology* **2015**, *43*, 247–250. [[CrossRef](#)]
139. Sambridge, M. Geophysical inversion with a neighbourhood algorithm—I. Searching a parameter space. *Geophys. J. Int.* **1999**, *138*, 479–494. [[CrossRef](#)]
140. Sambridge, M. Geophysical inversion with a neighbourhood algorithm—II. Appraising the ensemble. *Geophys. J. Int.* **1999**, *138*, 727–746. [[CrossRef](#)]

Disclaimer/Publisher’s Note: The statements, opinions and data contained in all publications are solely those of the individual author(s) and contributor(s) and not of MDPI and/or the editor(s). MDPI and/or the editor(s) disclaim responsibility for any injury to people or property resulting from any ideas, methods, instructions or products referred to in the content.